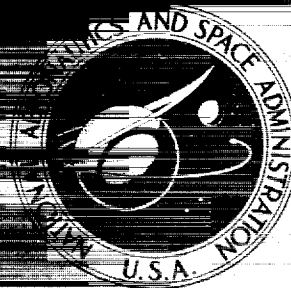


NASA TECHNICAL
MEMORANDUM



NASA TM X-1222

NASA TM X-1222

CLASSIFICATION CHANGES
UNCLASSIFIED

7 APR 1972

TP 72-165

Declassified by authority of NASA
Classification Change Notices No. 217
Dated ** 30 JUN 1972

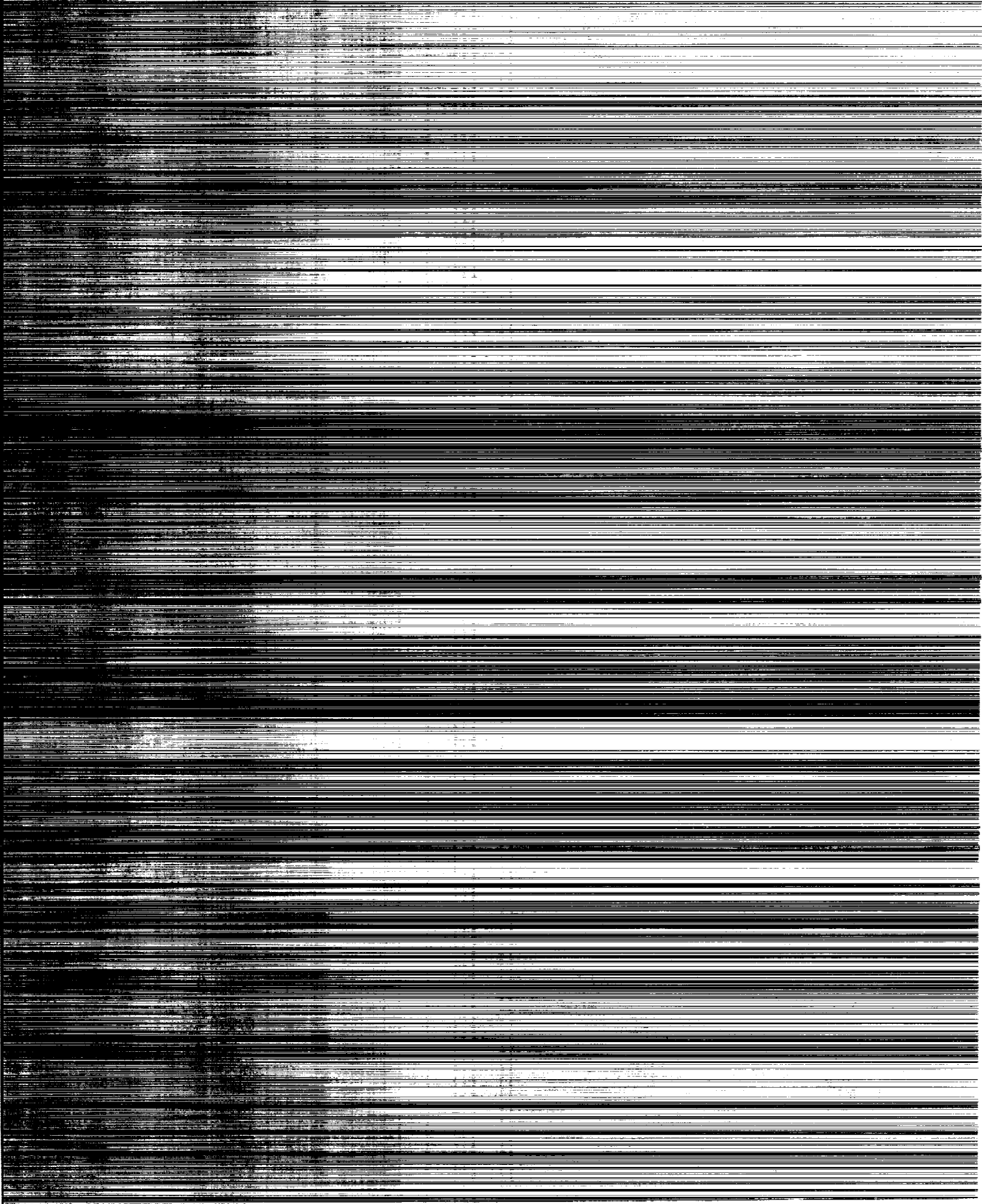
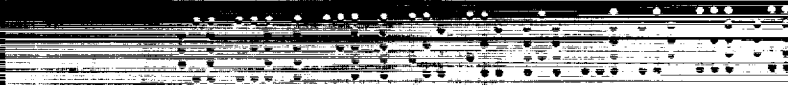
CASE FILE
COPY

PROJECT FIRE FLIGHT 1
RADIATIVE HEATING EXPERIMENT

by Dona L. Cauchon

Langley Research Center

Langley Station, Hampton, Va.

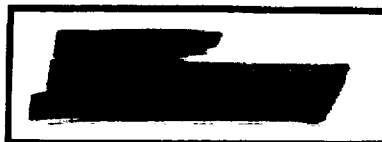


PROJECT FIRE FLIGHT 1 RADIATIVE HEATING EXPERIMENT

By Dona L. Cauchon

Langley Research Center
Langley Station, Hampton, Va.

[REDACTED]



[REDACTED]

NATIONAL AERONAUTICS AND SPACE ADMINISTRATION

[REDACTED]

03 12 2004

11/10/04

11/10/04

11/10/04

11/10/04

CONTENTS

SUMMARY	1
INTRODUCTION	1
SYMBOLS	2
EXPERIMENT DESIGN	7
Total Heating Experiment	7
Total Radiometers	7
Quartz Window Array	8
DATA REDUCTION AND ANALYSIS	9
Window Transmission	9
Exterior Window Heating	10
Shock-Layer Geometry	11
Program Assessment	11
RESULTS AND DISCUSSION	12
Radiometer Data	12
Forebody radiation	12
Afterbody radiation	14
Theoretical Predictions	15
Equilibrium and nonequilibrium radiation theory	15
Vacuum ultraviolet radiation	16
Atomic line radiation	17
Radiation-limiting phenomena	17
Comparison with theory	19
Flow-field studies	20
Calculation of shock standoff distance	22
Ground-Facility Experimentation	22
Total Heating Experiment	23
CONCLUSIONS	25
APPENDIX A - ERROR ANALYSIS	27
APPENDIX B - EFFECTS OF BODY MOTIONS ON STAGNATION HEATING RATES	34
APPENDIX C - RADIATION CALCULATIONS	37
REFERENCES	44
TABLE	47
FIGURES	50

037424J0001

037424J0001

[REDACTED] 11-551100

PROJECT FIRE FLIGHT 1 RADIATIVE HEATING EXPERIMENT*

By Dona L. Cauchon
Langley Research Center

SUMMARY

The Project Fire Flight 1 radiation experiment on a blunt Apollo-shaped reentry package yielded values of stagnation radiative heating that favored the lower boundary of theoretical prediction and ground facility experimentation.

The experimental results during conditions of early reentry allowed for some assessment of the radiation-limiting phenomenon of collision limiting. The portion of the experiment conducted near the peak heating period allowed for an adequate comparison with theory during periods of high radiative flux. With the use of data from the calorimeter experiments, observations are made on vacuum ultraviolet radiation and self-absorption. Body motions, unexpectedly experienced during the second and third experimental periods, were accounted for in order to adjust the data to conditions of zero angle of attack.

INTRODUCTION

For vehicles entering the earth's atmosphere from space, heat transfer becomes increasingly severe at velocities greater than 9 km/sec ($\approx 30\,000$ fps). In this velocity regime, radiation from the hot gases between the shock front and the spacecraft provides significant additional heating over and above that due to the frictional or convective mode.

One of the primary objectives of Project Fire was to determine the radiative heating to a large-scale blunt Apollo-shaped vehicle entering the earth's atmosphere at a velocity of approximately 11.3 km/sec (37 000 fps). The velocity is significant in that it represents a reentry condition more severe than that for Apollo and the flight measurements should provide valuable data anchor points with which to compare results from ground facilities and theoretical predictions. This velocity is also representative of minimum-energy earth reentries from the near planets. The large body size is particularly significant in that, up to the present time, the few "free flight" ground-facility experiments conducted at these velocities (Ames hypervelocity ballistic range) utilized only pellet-size models less than 2 cm in diameter. (See refs. 1 and 2.) When Project Fire was conceived, the range of agreement for some of the more prominent radiation theories (refs. 3, 4, and 5) was and still is of the order of four to one for certain flight conditions. The present state of

*Title, Unclassified.

[REDACTED]

the art does not allow experimental test facilities such as shock tubes and ballistic ranges to duplicate the combined temperature and density environment associated with flight conditions. (See refs. 1, 2, 6, and 7.) In light of this background, it was believed that a large-scale flight experiment would provide a needed definition of the radiative heating in this velocity regime. The results of such an experiment could well provide the anchor-point data necessary for selecting a proper theory for making more accurate predictions of radiative heating at these and higher velocities, including those associated with interplanetary return speeds.

Flight 1 of Project Fire was made from Cape Kennedy on April 14, 1964. It provided for a launch along the Eastern Test Range of a powered spacecraft mounted atop an Atlas D launch vehicle. After separation from the launch vehicle and orientation to the inertial reentry attitude, the spacecraft coasted to a point approximately 4000 int. n. mi. downrange. Here, at an altitude of about 305 km (1 000 000 ft), the reentry stage was spin stabilized and the Antares-II motor separated from the guidance components and ignited to provide a reentry speed of nearly 11.6 m/sec (38 000 fps). The 84-kg (185 lb) reentry package was then separated from the spent motor, which in turn was tumbled to increase its aerodynamic drag. For additional details concerning the flight prior to and during reentry, see reference 8.

The primary purpose of this report is to present the radiation data and deduced radiative heating rates for Flight 1. A preliminary analysis of the Project Fire data was presented in reference 9. Although a complete analysis had not been rendered at the time of that presentation, it was well suited as a status report and much of the presented material remains unchanged. On the other hand, the radiation data have been corrected as a result of a more recent evaluation of the radiometer calibration procedure and analysis of reentry package motions. Additional radiation theories and estimates based on experimental results are presented in this report, and more refined methods are used to obtain the theoretical heating rates from the flight trajectory.

SYMBOLS

A	area under stagnation nonequilibrium intensity profile between the shock and body, watts per centimeter ² (see fig. 11)
B ₁ , B ₂	constants (see eqs. (C11) and (C12))
c	velocity of light, 2.9979×10^8 meters per second
c _p	specific heat, Joules per kilogram-°K
D	Fire body diameter, centimeters
d _p	excitation distance, centimeters
d _{0.1}	relaxation distance, centimeters

E	flow energy, watts per centimeter ²
F _C	mean value of ratio $\frac{(\dot{q}_{C,\alpha})_{s/s_c=0}}{(\dot{q}_{C,\alpha=0})_{s/s_c=0}}$ over time interval of calorimeter data period
F _R	mean value of ratio $\frac{(\dot{q}_{R,\alpha})_{s/s_c=0}}{(\dot{q}_{R,\alpha=0})_{s/s_c=0}}$ over time interval of calorimeter data period
F _{cl}	collision-limiting factor (completely collision limited when F _{cl} = 0; no collision limiting when F _{cl} = 1)
\bar{F}_e	effective factor by which to "adjust" calorimeter stagnation data to the condition of zero angle of attack
h	altitude, kilometers (feet)
h	Planck constant, 6.6256×10^{-34} watts-second ²
I	radiation intensity, watts per centimeter ³
I _R	radiation steradiancy, watts per centimeter ² -steradian
I _e	equilibrium radiation intensity, watts per centimeter ³
I _o	predicted gas radiation intensity for flight conditions, watts per centimeter ³
K	rate constant, second ⁻¹ (see eq. (C17))
K ₁ , K ₂	constants (see eqs. (C11) and (C12))
k	Boltzmann constant, 1.38054×10^{-23} watt-seconds per °K
L _{dec}	characteristic length for decay, E/I _{st}
l	unit thickness of gas, centimeters
Δm	element dimension, meters
p	pressure, newtons per meter ² (microns of Hg)
\dot{q}	heating rate, watts per centimeter ²

CONFIDENTIAL

\dot{q}_C	convective heating rate, watts per centimeter ²
\dot{q}_R	local radiative heating rate, watts per centimeter ²
$\dot{q}_{R,M}$	predicted stagnation equilibrium radiative heating rate for a 1-cm thickness of gas using Meyerott's absorption coefficients, watts per centimeter ²
$\dot{q}_{ne,P}$	base stagnation nonequilibrium radiative heating rate obtained from reference 1, watts per centimeter ²
\dot{q}_t	total stagnation radiative heating rate (excluding vacuum ultra-violet) estimated for Flight 1, corrected for truncation and collision-limiting effects, watts per centimeter ²
\dot{q}_t^*	total stagnation radiative heating rate (excluding vacuum ultra-violet) estimated for Flight 1, corrected for truncation effects, watts per centimeter ² (see eq. (C25))
r_c	radius at corner, meters
r_n	body nose radius, meters
s	distance from geometrical stagnation point measured radially outward along the surface of the reentry package, meters
s_c	distance from geometrical stagnation point to corner measured radially outward along the surface of the reentry package, meters
T	temperature, °K
t	time, seconds
Δt	time increment, seconds
t_p	excitation time, seconds
$t_{0.1}$	relaxation time, seconds
U_s	shock velocity, kilometers per second
V	velocity, meters per second (feet per second)
$(V_{2,p})_{av}$	average velocity between shock front and excitation distance d_p , kilometers per second
$(V_{2,0.1})_{av}$	average velocity between shock front and relaxation distance $d_{0.1}$, kilometers per second

CONFIDENTIAL

W	Planck blackbody radiation intensity, watts per centimeter ² -steradian-micron
α	total angle of attack, degrees
α_{Be}	absorptance of beryllium
β	arbitrary optical property of quartz (see eq. (A1))
δ	shock standoff distance, meters
ϵ	emittance
θ	angle measured from longitudinal axis of reentry package facing forward and whose vertex is at center of curvature of spherical forebody, degrees
κ	thermal conductivity, Joules per meter-°K-second
λ	wavelength, microns ($1\mu = 0.001$ millimeter)
$\Delta\lambda$	wavelength interval, centimeters
μ_{λ}	spectral absorption coefficient, centimeter ⁻¹
ρ	density, kilograms per meter ³
$\bar{\rho}$	mean density between shock and body along stagnation streamline, kilograms per meter ³
σ	deviation
τ	true transmittance of fused quartz (see eqs. (1) and (2))

Subscripts:

aft	afterbody region (at radiometer location)
al	atomic line radiation
av	average
e	pertaining to equilibrium conditions
Fire	pertains to Flight 1 conditions
f	final conditions
fr	frozen
i	initial conditions

0112041

j	dummy variable (see eq. (1))
lab	laboratory reference
max	maximum
ne	pertaining to nonequilibrium radiation
o	sea level atmospheric conditions at Ascension Island reentry area ($T_o = 300^\circ \text{ K}$ (540° R); $\rho_o = 1.178 \text{ kg/m}^3$ ($7.345 \times 10^{-2} \text{ lbm/ft}^3$); $p_o = 1.01 \times 10^5 \text{ N/m}^2$ (2114 lbf/ft^2))
qtz	quartz
R	radiative
ref	reference conditions ($T_{\text{ref}} = 273.15^\circ \text{ K}$ (491° R); $\rho_{\text{ref}} = 1.295 \text{ kg/m}^3$ ($8.073 \times 10^{-2} \text{ lbm/ft}^3$); $p_{\text{ref}} = 1.01 \times 10^5 \text{ N/m}^2$ (2117.69 lbf/ft^2))
res	residence
s	location of offset radiometer measured along forebody surface from stagnation
st	stagnation region
trunc	referring to truncation
vuv	pertaining to vacuum ultraviolet radiation from O^+ and N^+ deioniza- tion continua in wavelength range between 0.04μ and 0.113μ
α	angle of attack
λ	wavelength
1	ambient condition in front of normal shock
2	equilibrium condition behind shock
(1),(2),(3)	designating maximum deviations (see appendix A)
∞	free-stream condition for flight

EXPERIMENT DESIGN

Total Heating Experiment

As discussed in reference 10, the Fire reentry package had a layered forebody construction consisting of three beryllium calorimeters interspersed with three phenolic-asbestos heat shields. The early reentry heating was monitored by the first beryllium layer until it reached its melting temperature. Provision was made to expose the second and third calorimeters at discrete times in order to measure, respectively, the heating near the middle (peak heating) and on the decreasing side of the heat pulse. The first two heat shields were provided to protect the second and third calorimeters until the designated exposure times. The third heat shield positioned behind the third beryllium calorimeter served to protect the main body of the reentry package after melting of that calorimeter.

The experiment plan was to monitor the total heating (the convective plus the absorbed radiative) using the calorimeters. Beryllium plugs, each containing four imbedded thermocouples at specified depths, were positioned at various locations in each calorimeter. (See fig. 1.) The forebody calorimeter data and the analysis of the forebody total heating have been reported in reference 10. Reference 11 presents the results of the afterbody experiments which included both temperature and pressure measurements and the afterbody heating analysis.

Total Radiometers

The gas radiation intensity was measured with onboard radiometers viewing the radiation through fused quartz windows. New clean windows were automatically provided with the exposure of the second and third beryllium calorimeters. The experiment plan was to subtract the measured radiative heating (adjusted for calorimeter surface absorption) from the total heating as determined by the calorimeters, the difference representing the convective heating plus the absorbed radiation outside the wavelength range of the radiometers. Radiation was monitored at three points on the reentry package. Figure 1 shows the positioning of these radiometers as well as other pertinent sensors on the reentry package. One total radiometer was positioned to view the radiation from the afterbody; a second total radiometer viewed the radiation from a location on the spherical front face offset 16° from the geometrical stagnation point; and a combined total-spectral radiometer was positioned to monitor the intensity of the plasma at the stagnation region.

The total radiometers were designed to monitor radiation in the wavelength range between 0.2μ and 6.0μ without spectral selectivity. The sensors were gold-black flakes mounted on thermopiles. The gold-black sensors, quartz optics, and MgF_2 coated aluminized mirrors which comprised the radiometer optics were assumed to provide a combined flat spectral response for these total instruments. This assumption was later checked out on tests on similar optical elements and the results of this study are discussed in appendix A. All three

total radiometers used in the experiment exhibited a dynamic response of approximately 3 decades of intensity without instrument saturation. The field of view of these instruments was about 10° (total included angle). These radiometers contained logarithmic amplifiers with direct signal output to the prescribed telemetry link for ground readout. The total radiometers were continuously monitored (not commutated), with provision for periodic inflight checking of telemetry zero and full-scale signals.

The spectral radiometer data are not included or discussed in this report.

Quartz Window Array

The radiometers viewed the radiating gas through fused quartz windows. (See fig. 2.) In the case of the stagnation and offset radiometers, the window array consisted of one window per calorimeter (total of three), one per heat shield (total of three) and one cover-plate window for a combined total of seven windows. The afterbody total radiometer viewed its radiation through one exterior window and one cover-plate window. Three different window thicknesses were involved:

Calorimeter and heat-shield windows	0.356 cm (0.140 in.)
All cover-plate windows	0.229 cm (0.090 in.)
Exterior afterbody window	0.711 cm (0.280 in.)

The transmittance of these window arrays is a function of wavelength and temperature. The data obtained by the radiometers therefore had to be adjusted for the optical behavior of these windows.

The exterior windows, that is, those subjected to the heating environment, were expected to be the most troublesome from the standpoint of temperature. Because of the low thermal conductivity of fused quartz, steep temperature gradients were manifested in these outer windows and the resulting effects on transmission had to be considered when analyzing the data. In determining the transmittance of these exterior windows, the temperature distribution in them was assumed to be induced by convective heating and the ultraviolet radiation to which the windows were opaque. This approach was justified by the fact that the absorptance of quartz in the wavelength range above 0.23μ is low and because the transmittance is essentially unaffected at window temperatures below 1645°K . (See fig. 3.) The effects of radiative heating on the temperature distribution within the outer quartz window were accounted for to some extent by considering the high conductivity characteristic (ref. 12) which essentially accounts for the radiation interchange within the quartz. In addition to resolving the optical behavior of the exterior windows, the temperature time histories through these windows were calculated in order to determine the useful transmission time for each of the three data periods. The radiation experiment was assumed to be terminated when the calculated surface temperature of the outer quartz window reached its melting point (approximately 1920°K).

DATA REDUCTION AND ANALYSIS

In general, there were two data reduction schemes available for reducing the Project Fire data: completely automatic reduction method and hand reduction method. A combination of the two, with greater emphasis on the hand reduction method, was used for the Flight 1 data. This method was dictated by the sporadic quality of the data which resulted from telemetry noise and dropouts.

The basic telemetry data from the total radiometers appeared as continuous voltage traces with time. Appropriate calibrations were applied to reduce these voltages to engineering units of radiation intensity of $\text{W/cm}^2\text{-sr}$ at the instrument. The calibration curves for the three radiometers are shown in figure 4. To these instrument readings were applied the necessary corrections for window transmission, exterior window heating, and gas cap geometry effects to convert the essentially normal irradiance sensed by the radiometers to the actual multidirectional gas radiation for properly assessing the heating effects on the surfaces of the calorimeters. These corrections are discussed in detail in the following sections.

Window Transmission

The irradiance of any total radiometer in the Fire experiment resulted from two sources: external gas radiation and self-emission from the hot external window in the array. In the case of a forebody radiometer, each of the above sources of radiation was attenuated as it passed through the window array. This attenuation due to reflections and absorption within the array is a function of both wavelength and temperature. In the machine program used for analyzing the Fire data, the wavelength dependence of the optical properties was considered throughout the window array, whereas the temperature dependence was considered only for the heated external window. The radiative flux absorbed by the cool rearward windows was not considered sufficient to raise the temperature of those windows significantly. Thus, the optical properties of the rearward windows were taken to be those of clear fused quartz at room temperature. In the machine program, the exterior window was subdivided into several elements, and transmission equations of the form

$$\begin{aligned} I_{R,j \rightarrow j+1} = & \left(I_{R,j-1 \rightarrow j} \tau_j \right)_{0.23 < \lambda < 1.2} + \int_{\lambda=1.2}^{\lambda=4.5} \epsilon_{j,\lambda} W_{j,\lambda} d\lambda \\ & + \int_{\lambda=1.2}^{\lambda=4.5} \left(I_{R,j-1 \rightarrow j} \right)_{\lambda} \tau_{j,\lambda} d\lambda \end{aligned} \quad (1)$$

were applied to each element. The notation $j \rightarrow j+1$ denotes the transfer of radiation from element j to element $j+1$. The intensity of radiation I_R

incident upon element j from the previous element has been divided into two separate wavelength regions. The gas radiation was assumed to occur at wavelengths less than 1.2μ and the quartz emission at wavelengths greater than 1.2μ . Thus, the three terms on the right-hand side of equation (1) account for the transmitted gas radiation, emission of the j th element, and the transmitted self-emission from the more forward elements. In equation (1),

$$(\tau_j)_{0.23 < \lambda < 1.2} = \frac{\int_{\lambda=0.23}^{\lambda=1.2} \tau_{j,\lambda} (I_{0,\lambda} \tau_{j-1,\lambda} \tau_{j-2,\lambda} \cdots \tau_{1,\lambda}) d\lambda}{\int_{\lambda=0.23}^{\lambda=1.2} (I_{0,\lambda} \tau_{j-1,\lambda} \tau_{j-2,\lambda} \cdots \tau_{1,\lambda}) d\lambda} \quad (2)$$

and

$$\epsilon_{j,\lambda} = (1 - \tau_{j,\lambda}) \quad (3)$$

In equations (1), (2), and (3), τ is a function of temperature and represents the true transmittance of the fused quartz within the medium. This particular optical property differs from the apparent transmittance values for a finite thickness shown in figure 3. The true transmittance values were deduced from the apparent transmittance values using the method outlined in reference 13.

Exterior Window Heating

In order to use properly the transmission equation (eq. (1)), it was necessary to know the temperature of the various subelements of the exterior window at each time during the experiment. The temperature time history for the j th window element was determined by applying a heat balance equation of the form

$$T_{j,f} = T_{j,i} + \frac{\Delta t}{\rho c_{p,j} \Delta m_j} \left[\frac{2(T_{j-1,i} - T_{j,i})}{\left(\frac{\Delta m}{\kappa}\right)_{j-1} + \left(\frac{\Delta m}{\kappa}\right)_j} - \frac{2(T_{j,i} - T_{j+1,i})}{\left(\frac{\Delta m}{\kappa}\right)_j + \left(\frac{\Delta m}{\kappa}\right)_{j+1}} \right] \quad (4)$$

where the terms in the brackets represent the "heat-in" and "heat-out" components due to conduction. The heat-in term for the first element was an assumed value of convective plus absorbed ultraviolet radiative heating. After determining the temperature and transmission through the window array, the radiative heating ($0.23 \mu < \lambda < 4.5 \mu$) on the body surface was deduced from the radiometer data. This value was subtracted from the total heating measured by the

SECRET

calorimeters, and the balance representing convective plus absorbed ultraviolet radiative heating was then used in an iterative procedure until the assumed and calculated values of this term agreed to within 1 percent.

Shock-Layer Geometry

The essentially normal steradiancy I_R from the shocked air sensed by the stagnation radiometer was converted geometrically by a factor of $2\pi(0.84)$ to account for the gas cap configuration. The value 0.84 was obtained from reference 14 and represents a correction to parallel plane geometry in order to more accurately account for the curvature of the shock layer. The assumptions made at this point in the analysis were those of a transparent and homogeneous gas volume and a concentric shock near the stagnation region. The same geometric factor was also used to reduce the offset radiometer data. The use of this factor introduced some error in the results for the offset radiometer because of deviations from concentricity of the shock and flow-field homogeneity near the corner. The problem of accurately determining such a factor is certainly formidable and especially so for conditions associated with nonequilibrium flow such as those estimated for the first data period. However, from purely geometrical considerations - that is, if the flow-field homogeneity assumption is maintained - the use of the geometrical factor $2\pi(0.84)$ can be shown to be reasonable for the offset radiometer position which is located at $s/s_c = 0.75$ ($\theta = 16^\circ$) on the front face for the first calorimeter experiment.

A geometrical factor of 1.26π was used for reducing the afterbody radiometer data. This factor is equivalent to that for a semicylindrical gas volume, given in reference 15, which has been assumed to be the radiating source for the afterbody.

Program Assessment

After the data were programed to obtain heating rates, one effect that had been expected to contribute substantially to the correction of the gas radiation measurements turned out to be surprisingly small. This was the temperature effect on the transmission of the outer window. The increase in attenuation due to window heating was indicated to be less than 1 percent in all three data periods; this was because of the fact that quartz transmission deteriorates only above 1645° K and that in all three data periods the rise from 1645° K to 1920° K (melting) occurred during periods of very high heating. These and the poor conductivity of quartz caused the window surface to cross that critical 275° K temperature span in a very short time; therefore, a sufficient thickness of the window was not allowed to be affected. Transmission, a function of window thickness as well as absorption coefficient, was in this case governed by the former. A second window phenomenon, emission, was calculated to have contributed about 4, 0.5, and 2 percent of the measured radiation, respectively, in the late stages of the first, second, and third data periods for the stagnation location.

RESULTS AND DISCUSSION

Radiometer Data

Forebody radiation.- Figure 5 shows the stagnation, offset, and afterbody radiation intensity data measured at the instruments plotted against elapsed time from launch ($h = 122$ km (400 000 ft) at $t = 1647.36$ sec). The stagnation results (fig. 5) are divided into the three experiment periods during which the data were gathered. In the analysis reported herein, the radiation experiments were considered to have been terminated when calculations indicated that the front exposed surface of the outer quartz window of the array reached a temperature of 1920° K.

During the first data period, the offset radiometer initially indicated slightly higher levels of radiation than the stagnation instrument. The onboard body motion sensors indicated conclusively that the reentry package was essentially at zero angle of attack at the start of the reentry and throughout this period. The higher levels of radiation intensity by the offset radiometer during the early reentry suggested strongly that this radiometer was more sensitive than the stagnation instrument at that time. The radiation levels at this time, however, were very low; hence, instrument accuracy was rather poor. Therefore, little significance could be attached to this difference between the two instruments. Before the first data period ended, the levels of radiation being recorded by the two instruments were comparable. Little justification existed for assuming either radiometer to be the more accurate and that the data afforded by each essentially represented boundaries of accuracy in this first data period.

The flight telemetry records indicated that during reentry at approximately 1665.9 sec (altitude = 70.4 km (230 540 ft), velocity = 11.5 km/sec (37 840 fps)), the reentry package was suddenly subjected to a severe impulse resulting in a moment about the center of gravity and unsymmetrical motions of the body with respect to the flight path. Two telemetry playbacks depicting this event are given in figure 6 (data from ref. 16). A postflight body motion study indicated that the stagnation radiometer periodically sensed radiation very near the aerodynamic stagnation region during the course of these body motions. The study, in fact, indicated that during the second data period, the reentry package was coning about an axis displaced approximately 17.5° from the flight path as shown in figure 7. The coning angle about this displaced axis was approximately 12° . During the third data period, these two angles were indicated to be 13° and 8.5° , respectively. These motions were such that the geometrical stagnation point of the reentry package (and therefore the stagnation radiometer) sensed its maximum radiation periodically and consistently at an angle of attack of approximately 5.5° during the second data period and 4.5° during the third data period. Prior to the onset of these motions, the two forward-looking radiometers were indicating an even rise in radiation intensity. After the impulse, these radiometers indicated oscillatory traces which, in general, were in phase with the motions of the body as derived from the onboard rate gyros and accelerometers, which are illustrated in figure 7. A curve was faired through the peak values indicated by the radiometers. (See fig. 5(b).)

The resulting values were then corrected to estimated stagnation point levels; this is explained in the following paragraphs.

Figure 8 indicates the radiative heating rate at the geometrical stagnation point of a blunt body for various angles of attack. The lower curve was faired using three points obtained from reference 17 for a body shape of $r_n/D = 1.00$. The other two theoretical points at 20° and 25° angle of attack were obtained from the Manned Spacecraft Center (MSC) for the Apollo shape ($r_n/D = 1.20$). The blunter Fire body approximates the Apollo shape with r_n/D ranging from 1.07 to 1.42 depending on the calorimeter or heat shield that is exposed. The Fire data points indicated in figure 8 were calculated from Flight 1 data that were obtained during an exceptionally clean portion of the telemetry record for the stagnation radiometer. These readings were obtained during the time when the first phenolic-asbestos heat shield ($r_n/d = 1.42$) was exposed. These points were deduced from the calculated angle-of-attack history illustrated in figure 7. The resulting data points definitely indicated a

higher trend showing a significant correlation of the parameter $\left(\frac{\dot{q}_{R,\alpha}}{\dot{q}_{R,\alpha=0}} \right)_{s/s_c=0}$ with bluntness r_n/D . A curve was then drawn through the Fire data points and

used to obtain the value of $\left(\frac{\dot{q}_{R,\alpha}}{\dot{q}_{R,\alpha=0}} \right)_{s/s_c=0}$ at the angles corresponding to the

peak points in the radiometer record. The method of determining this curve for $r_n/D = 1.42$ is given in appendix B.

Interpolating linearly between the three curves of figure 8 at $\alpha = 5.5^\circ$ and 4.5° for the second and third data periods, angle-of-attack correction factors for the respective bluntnesses in those periods ($r_n/D = 1.28$ and 1.07) were obtained. These correction factors, 0.94 and 0.93 for the second and third data periods, respectively, were then applied to the calculated heating rates which were based on the original radiation data that had been faired across the peaks of the oscillations, which represented conditions of angles of attack of 5.5° and 4.5° , respectively, for those data periods.

The maximum radiative heating rate obtained from the Fire stagnation radiometer data was 181.2 W/cm^2 at an elapsed time of 1671.1 sec during the second data period. This value was for approximate conditions of $h = 56.6 \text{ km}$ (186 000 ft) and $V_\infty = 11.1 \text{ km/sec}$ (36 530 fps) and is believed to be some 3 sec before peak heating.

Because of telemetry noise, no actual radiometer data were obtained during the third data period during the estimated useful window life. The values presented for this data period were taken from a curve faired across the peaks of the oscillations in the reduced radiometer record, and the values reported essentially resulted from bridging across this time interval from the portions of record on each side. These clean bracketing segments - that is, the portions

CONFIDENTIAL

unobscured by telemetry noise - may reflect radiation levels which include the effects of ablation products, especially in the earlier segment prior to the second heat-shield ejection time. The later portion corresponded to times when the third beryllium calorimeter was still intact and should be representative of a clean environment.

It was not possible to conduct any meaningful analysis on the offset radiometer during the second and third data periods, at which time body motions predominated. Because the roll rate gyro did not function during the flight, the time history of the position of the offset radiometer with respect to the flow field was indeterminate. A step function of the roll rate was assumed in the motions study; although this assumption did not appreciably affect the stagnation point motion, it could cause sizable errors in interpreting the motion of the offset radiometer. For this reason, the offset radiometer data were not considered in the second and third data periods.

As indicated earlier, the relationship between the offset and stagnation radiometer values in the first data period was distorted by an instrument sensitivity problem. Because of this problem, evaluating the distribution of radiative heating over the forebody of the Fire vehicle was not possible. A converse approach, however, did serve some meaningful purpose. A distribution factor representative of a cross section of current estimates of the radiation levels for the offset radiometer location was applied to obtain an independent assessment of the stagnation radiative heating.

The distribution of radiation over the forebody of the Fire reentry package (or similar blunt bodies) has been estimated by many authors (refs. 6, 14, 17, and 18). Additional distributions were determined from detailed flow-field studies (refs. 19, 20, and 21) procured under contract for Project Fire. Distributions from three sources (refs. 18, 19, and 21) are shown in figure 9. These three were chosen because they were calculated for the same flight condition which corresponded to a time prior to the onset of the body motions. Surprisingly, the agreement between the three distributions was not too good. As a result of this and in order to obtain the independent stagnation estimate, the calculated radiative heating rates for the offset radiometer location were

derived by using a factor, $\frac{\dot{q}_{R,s}}{\dot{q}_{R,st}} = 0.87$, which represented the average of the three distributions in figure 9 at that location.

The forebody heating rates are presented in figure 10 as heavy-line segments. The limits of precision of the Fire results were determined from an error analysis, which is included in appendix A.

Afterbody radiation.- The afterbody radiation experiment was not designed to periodically provide new clean windows during the reentry; as a result, the length of time of that experiment was dictated by the optical integrity of the 0.711-cm-thick (0.280 in.) exterior window and the possible but unknown effects of surface contamination from products of ablation.

[REDACTED]

As indicated in figure 5(a), the levels of radiation measured by the afterbody radiometer were lower than those indicated on the forebody. During the early reentry prior to the onset of the body motions, the afterbody radiation rise followed the forebody trend evenly but at some lower level. After the impulse at 1665.9 sec, the afterbody radiometer record indicated the same oscillating pattern and phase relationship as those for the forebody. More significant, however, was the fact that the mean (and peak) level of radiation decreased continuously from the time of impulse to the end of the reentry. This was unlike the forebody radiometer histories, which followed the characteristic radiation pulse through peak heating. This apparent ambiguity may have been the result of one or more of the following:

(a) Calculations indicated that the quartz window should have survived the reentry by a substantial margin. This "early peak" and decreasing level of radiation suggests strongly that the surface of the window may, however, have become contaminated by ablation products, which could have come from either melted beryllium, the forebody phenolic-asbestos, the afterbody coating, or the teflon band over the telemetry antenna.

(b) The body motions, ranging over angles of attack from 5° to 33° , caused a continuously varying flow field as exhibited by the oscillations in the radiometer record. As in the case of the offset instrument, the position of the afterbody radiometer under these flow conditions was indeterminate because of the lack of roll-rate information. The probability of the radiometer viewing some portion of the flow field other than that manifesting maximum radiative intensity is rather high.

(c) Because of the progressively changing shock shape and flow field through the reentry with time (even for zero angle of attack), the afterbody radiation may not remain necessarily a constant fraction of the stagnation radiation. As a result, the radiation history for the afterbody may peak at some time different from that for the stagnation region.

The maximum radiative heating rate calculated from the reduced Fire afterbody radiometer data was 1.6 W/cm^2 at 1665.9 sec (time of impulse). When the mean path length factor of 1.26, as suggested in reference 15 for the afterbody gas volume geometry, is used to reduce the measured irradiance to heating rates, a distribution factor calculated at 1664.4 sec from the Flight 1 data

indicated a heating distribution of $\frac{\dot{q}_{R, \text{aft}}}{\dot{q}_{R, \text{st}}}$ equal to 0.053 for the afterbody radiometer location.

Theoretical Predictions

Equilibrium and nonequilibrium radiation theory. - During hypersonic reentry, the flow field of the hot air behind a shock wave is said to reach equilibrium conditions when the temperature of the air reaches the point where the chemical composition of the gas is the same as the equilibrium composition at that temperature. Equilibrium radiation - that is, radiation from this air

[REDACTED]

CONFIDENTIAL

in chemical equilibrium - may be calculated from a theoretical evaluation of the absorption coefficients associated with the various molecular and atomic species and continua of air in the dissociated and ionized state. The resulting gas emissivity is generally a function of density and temperature.

Shock-tube experiments (ref. 6) on high-speed shocks in low-density gases indicate increased amounts or overshoot of radiation over the expected equilibrium levels in the hot gases immediately behind traveling shock waves. This increase has been attributed to the nonequilibrium condition of the gas in this region. A finite relaxation time is needed for the translational temperature of the gas to reduce to the equilibrium value from the much higher "ideal" value immediately behind the shock front. This relaxation time is dependent upon the chemical and excitation processes occurring in the nonequilibrium region; these processes, the result of two body collisions, in turn are functions of particle density. This same overshoot phenomenon has also been observed in high-speed ballistic range work. (See ref. 1.) A more extensive treatment of nonequilibrium radiation can be found in references 6, 22, and 23.

This increased radiation, due to nonequilibrium gas conditions, manifests itself in the hot gases behind the bow shock of a blunt body entering the earth's atmosphere and becomes significant during early entry under free-stream conditions of low density and high velocity. The distribution of radiation intensity between the shock wave and the body has the characteristic "overshoot" shape shown in figure 11. The relaxation distance $d_{0.1}$ is defined as the distance measured along the stagnation streamline from the shock to the point where the gas radiation intensity has reduced to 10 percent of the equilibrium level (point A). Point B identifies the peak radiation intensity of the nonequilibrium zone, and the distance from the shock front to this point is identified by d_p , the excitation distance. These dimensions, d_p , $d_{0.1}$, and the estimated shock standoff distance δ_{ne} , are considered basic to the calculation of the stagnation radiative heating rates. The nonequilibrium radiation (shaded area of fig. 11), based on the measurements of references 1 and 6, is approximately proportional to the fourth power of the flight velocity. The equilibrium radiation zone is that located between point A and the reentry package wall. The radiative heating directed to the body is the sum of the equilibrium and nonequilibrium components. Where self-absorption may be neglected, the radiative heating to the body is equal to the total integrated area under the intensity curve between the shock and the body.

Vacuum ultraviolet radiation.- Radiation is spectrally dependent. In the case of hot air radiation, the energy is distributed mainly over the spectrum from 0.04μ to 2.0μ . The radiation beyond these bounds is negligible. A source of radiation in high-temperature air due to the deionization continua of N^+ and O^+ has aroused increased interest in recent years. This radiation is most prominent in the wavelength range 0.04μ to 0.113μ . An early estimate of the radiance from these continua (ref. 4) indicated that at certain environmental conditions, the theoretical levels of radiation, which previously had been based on molecular and continuum radiation above 0.2μ , could be increased by as much as an order of magnitude. These estimates, however, were based on a sample thickness of 1 cm and the assumption of a transparent gas.

SECRET

Extension of this work to longer path lengths without consideration of absorption is invalid. Under certain conditions, even the thickness of 1 cm is a strong absorber. Absorption therefore tends to reduce the estimates of vacuum ultraviolet radiation to more modest levels such as those indicated in reference 24 which considers these phenomena. In the Fire experiment, the onboard radiometers, because of the wavelength cut-off of the quartz windows, were unable to sense this vacuum ultraviolet radiation. Because the beryllium calorimeters, however, absorb almost as a blackbody at these very low wavelengths, evidence of the existence of vacuum ultraviolet radiation would seemingly be indicated in these heating experiments. This will be discussed in more detail in the section entitled "Total Heating Experiment."

Atomic line radiation.- A still further source of radiative heating is atomic line radiation from nitrogen and oxygen. At temperatures above 9000° K and at densities normally associated with high-speed reentry, the radiation from atomic line transitions has been estimated to contribute a significant fraction of the total radiation. Allen (ref. 25) has included separate estimates of atomic line radiation at wavelengths longer and shorter than 0.2μ . That portion occurring at wavelengths longer than 0.2μ (principally in the spectral range between 0.7μ and 1.2μ), when added to the predicted radiation from molecular transitions and nitrogen and oxygen ion free-free and free-bound radiation above 0.2μ , provides a theoretical level of radiation with which the stagnation total radiometer data from the Project Fire reentry may be compared. The atomic line radiation below 0.2μ occurs roughly in the wavelength range between 0.14μ and 0.2μ .

Radiation-limiting phenomena.- Several phenomena have been described as being influential in decreasing the basic levels of radiation estimated for the reentry of a body into the earth's atmosphere. Some of the more important ones, defined in references 1, 6, and 17, as well as by other authors, include: truncation, collision limiting, self-absorption, and flow energy limiting.

In flight, truncation occurs when the condition of flow is such that the residence time a radiating particle exists in the nonequilibrium state is long and the corresponding relaxation distance along a streamline, based on the velocity distribution in the flow, is large compared with the shock detachment distance. For the stagnation streamline, the particle is swept away around the body without having reached equilibrium in the vicinity of the stagnation point. The total influence of the nonequilibrium radiation zone (fig. 11) is therefore reduced and the nonequilibrium radiation to the body is said to be truncated. The radiation distribution from the shock to the body at any location on the forebody may be determined fairly accurately by cross plotting radiation intensity distributions along streamlines (ref. 1) and the radiative heating to a point on the body surface may be determined by an appropriate integration over the gas volume. For a very blunt body such as Fire, the radiation distributions at nonequilibrium conditions along streamlines close to stagnation are very similar. The truncation effect at the stagnation region is therefore assumed to be predictable solely on the basis of the history of the stagnation streamline.

CONFIDENTIAL

Collision limiting is a second radiation-limiting phenomenon affecting the predicted radiation levels. It is prominent during early entry where the particle density in the shock layer is low and the number of collisions is not sufficient to maintain the population of excited states against the drainage by radiation. (See ref. 6.)

A correction factor accounting for this effect was applied to the theoretical estimates of total radiation which consist of both the nonequilibrium and equilibrium contributions. Based on the shock-tube experiments in reference 6 on one band system (N_2^+ first negative) at a velocity of 5.5 km/sec, it was demonstrated that there was essentially no collision limiting at ambient pressures down to 100 μ Hg. As pressure was further reduced, however, to 20 μ Hg, the collision limiting was observed to have reduced the intensity by one-half. Using these two conditions and assuming a logarithmic variation of collision limiting with density, the collision-limiting effects indicated by the straight-line relationship in figure 12 were applied to the Fire data. For reference,

$$\left(\frac{\rho_1}{\rho_0}\right)_{\text{Fire}} = 2.634 \times 10^{-5} \quad \text{corresponds to} \quad \text{Shock tube } p_1 = 20 \mu \text{ Hg}$$

$$\left(\frac{\rho_1}{\rho_0}\right)_{\text{Fire}} = 1.317 \times 10^{-4} \quad \text{corresponds to} \quad \text{Shock tube } p_1 = 100 \mu \text{ Hg}$$

When making reentry calculations involving radiation from hot gases having finite dimensions such as those between the bow shock and the reentry package, the transparent gas assumption has frequently been applied to molecular and continuum radiation. The assumption of a transparent gas means that there is no absorption in the shock layer. For most reentry conditions, this assumption is reasonable at wavelengths longer than 0.2 μ but is not necessarily valid at the shorter wavelengths. The strongly emitting deionization continua of N^+ and O^+ in the vacuum ultraviolet, for instance, are equally heavy absorbers. In the practical case, therefore, much of the estimated radiation based on reference 4 is absorbed and does not reach the body surface. Some absorption is also indicated for the atomic line radiation.

Flow energy limiting, sometimes referred to as radiation cooling or decay, is a further radiation-limiting phenomenon. The total flow energy entering the shock layer of the vehicle is given closely by

$$E = \frac{1}{2} \rho_{\infty} V_{\infty}^3 \quad (5)$$

If the drain of energy from the shock layer through radiation loss is a sufficient fraction of this total energy, the effect is such to reduce the gas temperature because of this decay of energy as the flow approaches the body. As a consequence, the intensity of radiation is reduced. On the basis of the characteristic decay length L_{dec} , suggested in reference 17, flow energy limiting

[REDACTED]

was not indicated to be a significant factor for the Fire reentry (table II); additional discussion on radiation cooling, however, will be included in the section "Total Heating Experiment."

Comparison with theory.- In figure 10, the values of the radiative heating rates to the body surface at the stagnation point deduced from the Flight 1 data are compared with predictions based on several prominent theories over comparable wavelength ranges. The five theoretical curves shown in figure 10 represent the combined contributions from the equilibrium and nonequilibrium modes of radiation. The equilibrium radiation was obtained from references 3, 4, 5, and 7. The nonequilibrium levels were deduced from reference 1.

Biberman and Norman (ref. 26) have indicated that the existing calculations of the N^+ and O^+ deionization continuum radiation, based on the hydrogen model, should be expected to overestimate the emission. It was pointed out in reference 7 that, for the flight conditions of the type experienced in Project Fire, the GE estimates (ref. 4), which utilized the hydrogenic model, were about a factor of 2 higher than those of reference 26 at conditions of extreme temperature. An additional correction to account for an increase in the overall radiation at the higher densities due to the N^+ photoattachment contribution suggested in references 27 and 28 is also included in reference 7. This contribution is very small, however, compared to the Biberman and Norman correction during the significant portions of the Fire reentry. Reference should be made to appendix C and table I for the methods employed and values obtained in estimating the total equilibrium and nonequilibrium radiative heating rates.

The range of theoretical prediction appears to be quite wide, the Fire data tending to favor the lower boundary and, in particular, the levels calculated using the absorption coefficients of reference 5 just prior to the peak heating portion of the reentry. Estimates of atomic line radiation obtained from reference 25 are presented in table I for the Fire reentry trajectory. Because of the late availability of reference 25, however, those estimates have not been included in the levels indicated by the theoretical curves shown in figure 10. Although the theory of Meyerott and coworkers appears to agree with the Fire results, the addition of atomic line radiation to this and to all the theories in figure 10 would tend to make the Fire results fall well below existing theoretical levels.

In the first data period, the instrument sensitivity problem has resulted in two interpretations of stagnation irradiance; one obtained from the actual stagnation radiometer readings and the other obtained from adjusting the offset radiometer readings to stagnation values for zero angle of attack with the use of an average estimated distribution factor. Although the data appear as a choice between the two sets of values, the spread is not nearly as wide as that resulting from the application and neglect of the empirical collision-limiting estimate of reference 6 to the theory of Meyerott et al. in figure 10. A truncation correction has also been included in the adjustment of the basic nonequilibrium radiation estimate. (See calculations in appendix C.) For a reentry like that of Project Fire, collision limiting appears to be the dominant radiation-limiting phenomenon during the early reentry completely negating any effect attributable to truncation.

[REDACTED]

CONFIDENTIAL

A collision-limiting relationship was deduced from the data obtained during the early part of the Fire reentry. An average of the reduced stagnation radiative heating results from the two forebody radiometers was divided by the theoretical values obtained using references 1 and 5 without collision limiting during the first data period. The resulting calculations indicated that the collision-limiting factor F_{cl} may be closely approximated by the linear relationship

$$\left. \begin{aligned} F_{cl} &= 2.5 \times 10^4 \left(\frac{\rho_1}{\rho_0} \right) & \left(\left(\frac{\rho_1}{\rho_0} \right) \leq 4.0 \times 10^{-5} \right) \\ F_{cl} &= 1.0 & \left(\left(\frac{\rho_1}{\rho_0} \right) > 4.0 \times 10^{-5} \right) \end{aligned} \right\} \quad (6)$$

which is plotted in figure 12. Calculations were not considered prior to the elapsed time of 1663.0 sec because estimates of conditions of severe truncation strongly influence the theoretical levels at those times. In addition, the Fire data, because of the differences between the two forebody radiometers, may well be less reliable for use in this type of calculation. The collision-limiting relationship based on the measurements of reference 6 for the N_2^+ (first negative) species and used in appendix C is shown for comparison.

The following table summarizes the relative agreement between the Fire measurements and the estimated radiative heating rate at representative times during each data period:

Data period	Time, sec	Fire 1 data, W/cm ²	Estimated Fire 1 levels* (refs. 1 and 5), W/cm ²
First	1664.4	16.5	10.7
Second	1670.5	151	144
Third	1677.0	37.2	72.5

*Adjusted for collision limiting and truncation (see appendix C).

The values in the preceding table were for the wavelength range from 0.23 μ to 4.5 μ . The Fire data were corrected for window transmission and self-emission, gas cap geometry, and body motions.

Flow-field studies.- Included in figure 10 are heating estimates at discrete points in the reentry that were determined from the previously mentioned flow-field studies (refs. 19, 20, and 21). These calculations were based on the nominal preflight Fire 1 reentry trajectory and the 1962 U.S. Standard Atmosphere (ref. 29). Because of the approximate nature of the trajectory and atmosphere submitted to the three contractors for use in their studies, the

CONFIDENTIAL

[REDACTED]

positioning of their points in figure 10 may be slightly in error. The conditions of flight for which the analyses were made were

For equilibrium flow:

Altitude = 52.3 km (171 611 ft)

Velocity = 10.5 km/sec (34 582 fps)

For nonequilibrium flow:

Altitude = 79 km (259 113 ft)

Velocity = 11.4 km/sec (37 439 fps)

The Flight 1 velocities at the same two altitudes were about 0.18 km/sec (600 fps) faster than these preliminary estimates. Stainback (ref. 18) performed calculations at slightly different flight conditions for nonequilibrium flow. As previously mentioned, the 1962 U.S. Standard Atmosphere (ref. 29) was used in these studies. The atmospheric conditions used to obtain the various theoretical curves in figure 10 were taken from actual soundings (ref. 16) obtained at Ascension Island 4 hours after the flight. These two atmospheres, incidentally, were remarkably alike. The stagnation radiative heating rates from the flow-field studies are shown in the following table:

Source	Predicted stagnation radiative heating rates, W/cm ² , for -	
	Equilibrium flow	Nonequilibrium flow
GE (ref. 20)	363 (0.16 μ < λ < 10 μ) 1248 (0.05 μ < λ < 10 μ)	
Philco (ref. 21)	*367 (0.0685 μ < λ < 5.0 μ)	6.0 (0.0685 μ < λ < 5.0 μ)
Lockheed (ref. 19)	*425 (0.05 μ < λ < 10 μ) 211 (0.1167 μ < λ < 1.98 μ) (based on ref. 5) 725 (0.2 μ < λ < 10 μ) (based on ref. 3) 1860 (0.05 μ < λ < 10 μ) (based on ref. 4)	96.0 (0.062 μ < λ < 2.0 μ) (upper bound) 30.0 (0.062 μ < λ < 2.0 μ) (lower bound)
Stainback (ref. 18)	465 (0.2 μ < λ < 10 μ) (based on ref. 30) 670 (0.2 μ < λ < 10 μ) (based on ref. 3) 1071 (0.05 μ < λ < 10 μ) (based on ref. 4)	

*Self-absorption in the gas is considered.

[REDACTED]

CONFIDENTIAL

Calculation of shock standoff distance.- Inasmuch as Project Fire was an experiment designed to measure heating rate, the conversion to gas radiation intensity in W/cm^2 would necessarily entail the determination of the shock detachment distance. The value used for the predictions outlined in figure 10 was a blunt-body approximation deduced from the method of Kaattari (ref. 31); namely,

$$\delta_e = \frac{3}{4} \frac{\rho_1}{\rho_2} r_n \quad (7)$$

This equilibrium value was adjusted for nonequilibrium effects where applicable. (See assumptions and method in appendix C.)

Where gas absorption is negligible, the stagnation-point radiative heating rate is almost directly proportional to the shock standoff distance except where strongly influenced by nonequilibrium effects. From the flow-field studies substantial differences appear to exist between the values of shock standoff distance calculated by the various methods. In addition to that obtained by the method of appendix C, the values of shock standoff distance that resulted from the four flow-field calculations previously described were:

	δ , cm
For equilibrium flow:	
GE (direct Gravalos method), reference 20	4.03
Lockheed (inverse Swigart method), reference 19	4.45
Philco (direct Dorodnitsyn method), reference 21	3.68
Stainback, reference 18	4.01
Method of appendix C	3.87
For nonequilibrium flow:	
Lockheed, reference 19	3.92
Philco, reference 21	5.64
Stainback, reference 18	4.06
Method of appendix C	Approx. 4.12

Ground-Facility Experimentation

Measurements of gas radiation levels have been made in ground facilities such as shock tubes and ballistic ranges. (See, for example, refs. 1, 6, 7, 32, and 33.) The results from the various experiments fall mostly in the range between the levels predictable by the theories of Kivel and Bailey (ref. 3) and GE (ref. 4) for air radiation above 0.2μ .

At first glance, the results of ground-facility experimentation appear to indicate higher levels of radiation than those measured in the Fire experiment because they favor the higher valued theories; however, this may not necessarily be true. The combined thermodynamic conditions of density and temperature of the shocked gas associated with the Fire reentry (table I) have not been duplicated as yet in ground facilities. Therefore, the Fire experiment should not

CONFIDENTIAL

~~CONFIDENTIAL~~

be used to correlate in any rigorous manner the results of ground facility tests. The flight results in effect extend the range over which measurements have been made, and actually complement the ground facility efforts in exploring these high-enthalpy phenomena. Considering the Fire results in this light, it may be possible to obtain information on trends and/or deficiencies in the various theoretical methods as the range of thermodynamic properties over which testing is conducted is extended by such flight experiments.

Total Heating Experiment

The stagnation total heating rates for Fire 1 are shown as bands in figure 13, the spread in the results reflecting the available choice in fairing the calorimeter temperature time histories. Correction factors to account for the deviations in both the convective and absorbed radiative heating components due to the body motions (see appendix B) were applied during the second data period to the heating rates that were reported in reference 10. The final resulting total heating rates, adjusted to the condition of zero angle of attack, are indicated in figure 13 by the heavier cross-hatched area. The Fire heat flux was due to the convective plus absorbed radiative heating at the beryllium calorimeter surface. Were it possible to have spectrally measured all the radiation from the gas cap by the radiometers, the convective and radiative heating rates could easily have been assessed separately by just subtracting the integrated absorbed radiative component from the total heating rates. This was not the case, however. Radiation is spectrally dependent, and the wavelength cut-off of the quartz windows essentially dictated limits on the amount of gas radiation incident at the body surface that was actually sensed by the radiometer.

In order, therefore, to attempt to distinguish between the various modes of heating contributing to the measured calorimeter fluxes, a representative convective heating rate based on the Fire trajectory was calculated. The theory of Cohen (ref. 34) was used. In the absence of perturbing phenomena such as vorticity interactions and coupling effects with radiation, this estimate of the convective heating is reasonable. The difference between it and the total heating results should represent a measure of the absorbed radiation over the complete spectrum. The calorimeter experiment during the second data period of Project Fire (i.e., near peak heating) is particularly noteworthy. If the measured radiation from Fire (i.e., at wavelengths greater than 0.23μ) is adjusted to account for the absorptance of the beryllium calorimeters and added to the calculated Cohen convective heating, it can be seen that the resulting energy is not sufficient to account for the difference between the convective heating and the total heating levels measured on the calorimeters. The evidence is strong that the remaining difference is due to atomic line radiation and/or radiation from the deionization continua of N^+ and O^+ outside the measurable wavelength range of the stagnation radiometer, that is, below 0.23μ . Only the possibility of an abnormally high convective heating rate would preempt this conclusion. In order to show the extent to which the Fire measurements are predictable with the use of certain available analytical methods, a theoretical estimate of the total stagnation heating rates for the Flight 1 reentry trajectory is indicated along with the experimental results in figure 13. The theoretical estimate is the sum of:

~~CONFIDENTIAL~~

- CONFIDENTIAL
- (1) Convective heating (ref. 34) utilizing the equilibrium values of the thermodynamic properties of the shocked gas throughout the trajectory
 - (2) Radiation (ref. 5) in the wavelength range from approximately 0.115μ to 2.0μ adjusted for beryllium absorptivity
 - (3) Vacuum ultraviolet radiation (which includes self-absorption effects, ref. 24) for the wavelength range from 0.04μ to 0.113μ to account for the radiation from the N^+ and O^+ deionization continua
 - (4) Atomic line radiation (which includes self-absorption effects, ref. 25) in both the ultraviolet and infrared regions of the spectrum approximately adjusted for beryllium absorptivity
 - (5) Nonequilibrium radiation estimates based on the experimental work of reference 1

It should be observed that these heating sources represent but one combination of theoretical estimates that may be used to predict the total heating for the Fire reentry. Care should be exercised in making any final conclusions about the complete heating story as a result of the Fire experiment. Different estimates of the contributions from the above sources are certainly possible within the framework of present-day theory and probably would still be compatible with the Fire results.

The theoretical approach need not necessarily be restricted to the sources of heating outlined in the aforementioned estimate. Differing opinions on radiation-limiting phenomena and interactions between convective and radiative heating may lead to equally defensible theories on reentry heating. In considering, for instance, the first data period (fig. 13), the estimated ultraviolet radiation below 0.23μ is low and essentially unabsorbed within the gas and does not account for the difference between the Fire results and the convective heating theory. On the other hand, if consideration is given to the effects of vorticity interactions between the shock and boundary layers, which have been predicted by several investigators and which were incorporated in the flow-field studies (refs. 19 and 21), the conventional estimates of convective heating (e.g., ref. 34) could be increased by as much as 30 percent depending upon the particular vorticity theory considered. The Fire environmental conditions during early reentry in the first data period, which are characterized by Reynolds numbers of the order of 10 000, do in fact correspond to those conditions at which such increased levels are predicted.

During the second experimental period, vacuum ultraviolet radiation and gas absorption are prominent. Radiation cooling and subsequent decreases in shock-layer enthalpy could be limiting from the standpoint of both the radiative and convective modes of heating. Vorticity effects are not important at these times. The substantial differences between the theory used and the Fire results in the second data period may either lie in the theoretical levels themselves or in the methods by which self-absorption is considered or be the result of interactions between the radiative and convective modes of heating.


[REDACTED]

Using the Fire results and guided by existing theoretical estimates, therefore, it is possible to attempt to assess the various modes of heating associated with the Fire reentry. The final work, however, on the contributions from these sources can only really be surmised because of the inability of the Fire experiment to uniquely distinguish between them.

CONCLUSIONS

The conclusions presented herein are based primarily on the results of radiation measurements obtained during the Project Fire Flight 1 reentry heating experiment. This experiment utilized a relatively large-scale blunt Apollo-shaped body reentering the earth's atmosphere at an initial velocity of approximately 11.6 m/sec (38 000 fps). An analysis of the data indicates the following conclusions:

1. The stagnation total radiometer data for the wavelength range between 0.23μ and 4.5μ indicate that the stagnation-point radiative heating rates encountered during the Flight 1 reentry favored the lower boundary defined by current theoretical prediction methods. Specifically, the levels deduced by using equilibrium theory of Meyerott et al. (AFCRC-TR-59-296), adjusted by radiation-limiting considerations and nonequilibrium estimates of Page and Arnold (NASA TR R-193), were in reasonable agreement with the Fire 1 results in all data periods. If the radiative heating theory above 0.23μ is enhanced by estimates of atomic line radiation, the theory overestimates the Fire results by better than a factor of 2.
2. The stagnation radiometer record in the second data period prior to peak heating, although indicating an oscillatory trace because of body motions, was reduced to stagnation-point radiative heating for zero angle of attack. This reduction was achieved following a study of the body motions, and the subsequent analysis of the flight data provided corroboration for theoretical calculations of the radiative flux at the center of the heat shield as a function of angle of attack.
3. The maximum radiative heating rate deduced from the afterbody radiometer data was 1.6 W/cm^2 at 1665.9 sec. A distribution factor calculated at 1664.0 sec indicated that the radiative heating rate at the afterbody radiometer location was equal to 0.053 times the stagnation value. The afterbody radiometer data were suspected to be unreliable after the onset of the body motions.
4. Collision limiting appeared to be a dominant radiation-limiting factor during the early part of the Fire 1 reentry. Because of the reentry time at which it is influential, it apparently negates any effect that might be attributed to truncation. An estimate of the radiation attenuation due to collision limiting, as deduced from the Fire 1 data, is proposed.
5. Evidence afforded by consideration of the calorimeter experiment in conjunction with the radiometer experiment for the stagnation region strongly


supports the fact that substantial heat flux to the Fire vehicle was due to vacuum-ultraviolet radiation (wavelengths less than 0.2μ).

6. If the convective heating experienced by the Fire reentry package is assumed to be reasonably predicted by the method of Cohen (NASA TR R-118), evidence afforded by consideration of the calorimeter flux indicates that theoretical methods of predicting total heating, which include the vacuum-ultraviolet contribution and the effects of self-absorption, are in general agreement with the flight measurements. The Flight 1 reentry heating experiment, however, does not allow for any conclusive statement concerning the contributions from each mode of heating, the various sources of ultraviolet radiation, and the effects of radiation cooling and absorption in the gas.

Langley Research Center,
National Aeronautics and Space Administration,
Langley Station, Hampton, Va., December 8, 1965.

APPENDIX A

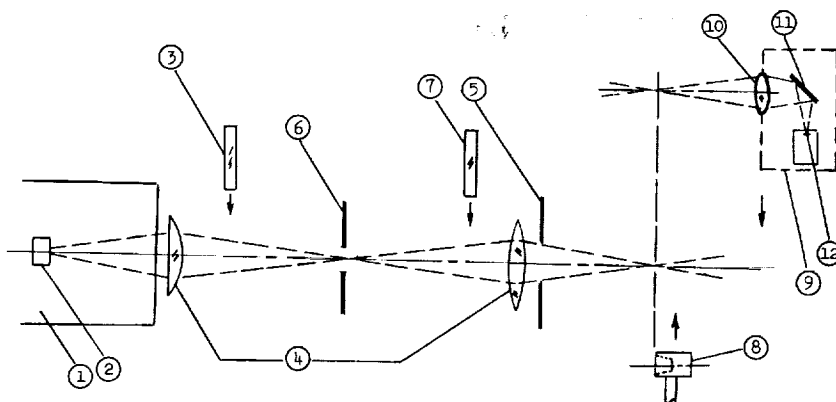
ERROR ANALYSIS

The precision to which the Flight 1 radiative heating rates shown in figure 10 were finally reduced was affected by several factors. Three areas of the reduction and analysis were estimated, however, to provide the major elements of uncertainty in the Fire results: (1) radiometer calibration method, (2) readability of the reduced data, and (3) flight telemetry error. An error analysis to ascertain the limits of accuracy for the radiative heating rates is presented in this appendix. The discussion is presented in some detail in order to give the reader some insight into some of the problems involved in considering flight experiments to measure radiation from high-intensity sources.

Radiometer Calibration Method

Calibration setup and procedure.- The total radiometers for Flight 1 were calibrated in $\text{W/cm}^2\text{-sr}$ against output voltage. The calibration curves for the three radiometers shown in figure 4 were obtained in the manner described in the following paragraphs.

An optical bench was alined as indicated in the following sketch which shows the radiometer calibration setup:



- | | |
|-----------------------------|---|
| ① Inert gas furnace (argon) | ⑧ Intensity-measuring lampblack thermocouple with galvanometer and associated readout equipment |
| ② Carbon block source | |
| ③ Screen filter 1 | ⑨ Radiometer to be calibrated |
| ④ Focusing lens pair | ⑩ Focusing radiometer lens (quartz) |
| ⑤ Variable iris aperture | ⑪ MgF_2 coated aluminized quartz mirror or beam splitter |
| ⑥ Glare stop | |
| ⑦ Screen filter 2 | ⑫ Radiometer sensor - gold black thermopile |

Sketch 1

APPENDIX A.

The optics were alined to produce an image of the carbon block source ② at some suitable point in the train. The irradiance at the image was measured with the thermocouple ⑧. The absolute calibration steradiancy was calculated with the use of this measurement and the geometry of the optical system. The thermocouple was then removed to allow the radiometer to be moved into position as indicated in sketch 1 in order to view the same steradiancy as that viewed by the thermocouple. A necessary geometrical consideration was that the view angle of the instrument be completely flooded by the incident light.

Because it was not possible to monitor the higher levels of radiation intensity from the carbon block source without damaging the thermocouple, the procedure was modified in order to calibrate the total radiometers at the higher intensity levels. During the time that the thermocouple was being used, screen filter 1 ③ was continuously in place to protect the thermocouple from overheating; its transmission factor was approximately 2.2 percent. When calibrating the upper two decades of the dynamic range of the total radiometers, the thermocouple was removed and the intensities obtained by calculating the transmission factor of the screen combinations in positions ③ and ⑦. These screens had been previously calibrated in a spectrophotometer and their transmission assumed to be spectrally flat and accurately known. The radiometer again was permitted to view the radiation at each filter setting in order to obtain its output voltage with respect to the calculated incident steradiancy.

Smoothing of calibration curves.— The resulting data points of the calibration procedure were smoothed for plotting by dividing the measured (or calculated) intensities at the image plane by the transmission factors of the combined screen filters. Theoretically, if it is assumed that the carbon block source did not vary in temperature (and intensity) over the period of a single instrument calibration, this calculation should yield the same value of source energy. Scatter, however, was noted in these calculated values. An average source value was computed and this value multiplied by the transmission factors of the filters to obtain "adjusted" intensity values. The approach is indicated in the following sample calculation:

(1) Reading	(2) Intensity measured (or calculated) at the image plane, W/cm ² -sr	(3) Transmission factor of filter combination	(4) Calculated source intensity, (2)/(3), W/cm ² -sr	(5) Average of column (4)	(6) Adjusted intensity value, (3) × (5), W/cm ² -sr
1	10	0.15	66.7	66.4	9.96
2	20	.32	62.5		21.2
3	35	.50	70.0		33.2

Based on the final preflight calibrations of the three flight instruments, the deviations from column (2) exhibited in column (6) were indicated to be

APPENDIX A

$$\sigma = \pm 4 \text{ percent}$$

which reflects the maximum estimated uncertainty in the steradiancy levels because of this smoothing approach.

Postflight evaluation.- A second consideration dealt with certain questionable details of the Flight 1 calibration procedure, which were investigated in a postflight evaluation of the techniques used. This study revealed the following:

(a) Linearity correction: The right-hand focusing lens of the lens pair (sketch 1, component ④) converged the energy onto the thermocouple ⑧. Because the iris aperture, component ⑤, was not properly closed down, the thermocouple was permitted to view the radiant flux transmitted over the full area of this right-hand lens. In the steradiancy calculation, the assumption had been made of constant energy distribution over this lens area. This assumption was found to be incorrect; in fact, the distribution of energy across the dimensions of that lens was found to be strongly nonlinear. During the calibration the radiometer with its narrow beam viewed the carbon block source through only a small area at the center of the lens where the distribution was reasonably linear. The intensity-measuring thermocouple, on the other hand, gave readings that reflected an average steradiancy from the entire flux converging upon it from the complete lens area. The degree of nonlinearity in the steradiancy was determined by using various aperture openings of the iris diaphragm and by measuring the thermocouple output. These measurements of nonlinearity indicated that the actual steradiancies seen by the instrument during calibration were between 45 and 55 percent higher than the calculated average steradiancies.

(b) Thermocouple housing: The intensity-measuring thermocouple sensor was housed in a tapered conical cavity whose reflecting and reradiating walls contributed to a significantly higher energy input to the sensing element than would normally be incident upon it without this housing. The thermocouple sensitivity determined by the vendor was for the sensing element mounted in its housing so that reflection and reradiation effects were included. The radiometer calibration setup shown in sketch 1 was such that the converging flux from the right-hand lens fell directly on the sensor with little or no energy impinging upon the sidewalls. The result was that the steradiancy levels calculated in the preflight calibrations were low by between 20 and 28 percent in addition to that error indicated in (a). This deviation was confirmed by tests run with both the vendor and calibration setups with and without "flux-wetting" the sidewalls.

Combining the effects of (a) and (b), the total range of uncertainty due to calibration anomalies was calculated to be:

$$\text{Maximum deviation} = 1.53 \times 1.28 = 1.96$$

$$\text{Minimum deviation} = 1.45 \times 1.20 = 1.74$$

APPENDIX A

The steradiances were actually adjusted by a factor of 1.88 in the final analysis. This was a weighted average value based on tests conducted where a radiometer was calibrated by using, first, the original procedure and, then, a modified procedure that eliminated the errors discussed in (a) and (b). The maximum possible deviations applicable therefore to the final heating rate analysis were:

$$\sigma_+ = \frac{0.08}{1.88} = 4 \text{ percent}$$

$$\sigma_- = \frac{-0.14}{1.88} = -7 \text{ percent}$$

Spectral response of components. - A third factor affecting the accuracy of the final heating rate values and attributed to the radiometer calibration procedure deals with the spectral response of several of the individual optical elements of the total radiometer. To some extent, the spectral response of certain elements of the optical train are also involved.

An unfortunate shortcoming of the calibration procedure for the Fire radiometers was the impossibility of duplicating in the laboratory the spectral distribution of the gas radiance to which the instrument would be subjected in flight. The carbon block source used in the laboratory calibration was heated to approximately 2500° K, whereas the anticipated gas radiance would constitute a source at about 11 000° K. The Planck distributions for these two temperatures peak at 1.2 μ and 0.26 μ, respectively. This fact pointed to the need for optical elements exhibiting a flat (constant) spectral response over the complete spectrum down to 0.23 μ if the calibrations conducted on an infrared source were to be meaningful. In applying the radiometer calibrations, it was assumed that the pertinent optical components of the system were gray, that is, exhibiting this constant optical response over the spectral range between 0.23 μ and 4.5 μ. The components of the calibration setup and radiometer that were particularly involved were those beyond the last converging lens and included ⑧, ⑩, ⑪, and ⑫. (See sketch 1.) The degree to which these departed from complete spectral flatness would in effect determine the precision of the final reduced Fire data. The lampblack coating of the thermocouple, element ⑧, and the gold black flake of the radiometer thermopile, element ⑫, were estimated to be gray within 5 percent ($\sigma = \pm 5$ percent for the combined effect of both sensors) over the wavelength range from 0.23 μ to 4.5 μ. The effects of the quartz optics of the radiometer system were slight. In both the calibration setup and the flight case, the original source radiation (whether carbon block or radiating air) was already strongly filtered and spectrally shaped by the preceding quartz optics in the spectral regions of consequence for the quartz lens, depending upon the system. As a result, equations of the form

$$\beta_{av} = \frac{\int_{0.23}^{4.5} (\tau_{qtz} I_o)_{\lambda} \beta_{\lambda} d\lambda}{\int_{0.23}^{4.5} (\tau_{qtz} I_o)_{\lambda} d\lambda} \quad (A1)$$

where β is a characteristic optical property of the fused quartz, indicated that the effects of the absorption bands of the external fused quartz optics under both the calibration and the flight conditions were such as to greatly deemphasize the influence of the source radiation in those wavelength regions. In flight, it was determined that due to this effect, the radiometer readings were 3 percent too high.

The remaining element of the radiometer that could cause any significant error in the measured data because of variations in optical properties over the wavelength range from 0.23 μ to 4.5 μ would be the MgF_2 coated aluminized quartz mirror or beam splitter (the stagnation instrument employed a beam splitter to share the energy with the spectral radiometer at the same location). This optical element would cause discrepancies in the flight data for the same reasons as those of the internal quartz optics previously described - that is, because of the spectral difference between the calibration and flight intensity sources. The actual flight mirrors were never tested. Standard commercial reflectance values for similar elements indicated, however, that due to this effect, the radiometer readings were low by about 5 percent for the mirrors but by some 15 percent for the beam splitter. These values were based on an assumed broadband spectral distribution of the gas radiation (ref. 25).

The deviation attributable therefore to varying spectral response of radiometer components would be

Stagnation radiometer	{ +21 percent - 8 percent
Offset and afterbody radiometers	{ +10 percent - 8 percent

Combining all the effects discussed, the final limits of precision applicable to the Flight 1 data due to uncertainties in the radiometer calibration procedure were

Stagnation radiometer $\sigma(1)$	{ +31 percent -18 percent
Offset and afterbody radiometer $\sigma(1)$	{ +19 percent -18 percent

These maximum deviations are applicable to all three radiometers and all three experimental periods.



Readability of the Reduced Data

The maximum errors possible in reading the flight record reduced to engineering units were estimated to be

Instrument	Maximum deviation, $\sigma_{(2)}$, for -		
	First data period	Second data period	Third data period
Forebody radiometers (stagnation and offset)*	± 10 percent	± 10 percent	± 30 percent
Afterbody radiometer	± 10 percent		

*Offset radiometer deviations applicable to first data period only.

These estimated errors were based on the levels of telemetry noise and the extent to which extrapolations and interpolations from and between good pieces of record through areas of signal dropout were needed in order to predict levels in the three data periods. The bracketing data from which the fairing for the third experimental period was determined were obtained from radiation levels that reflected in part the contribution of ablation products and which were obtained at times when it was difficult to distinguish between the data and the telemetry noise during much of this time.

Flight Telemetry Error

The accuracy of the telemetry system utilized in Project Fire has been estimated to be within ± 2 percent for the radiometer data. This deviation for the bandwidth corresponding to 5 V full scale indicated therefore that the data recorded at the ground receiving stations were accurate to within ± 0.1 V. The radiometer calibration curves (fig. 4) indicate the following deviations for the three radiometers in the various experiment periods:

Instrument	Maximum deviation, $\sigma_{(3)}$, for -		
	First data period	Second data period	Third data period
Stagnation	± 15 percent	± 15 percent	± 20 percent
Offset	± 10 percent		
Afterbody	± 15 percent		

These values were dictated by the slopes of the various calibration curves during the times of the experimental periods when the data were obtained.

APPENDIX A

An additional error of ± 25 percent was estimated to be possible for the afterbody heating rates because of the use of the approximate geometric factor of 1.26 obtained from reference 15 in the analysis of those data.

The maximum deviations for the three main areas of data reduction and analysis were then combined into a final maximum deviation reflecting the overall precision of the data presented in figure 10 for the forebody radiometers. Maximum deviations for the afterbody heating rates are given in the following table:

Instrument	Maximum deviation, σ_{\max} , for -		
	First data period	Second data period	Third data period
Stagnation	{ +65 percent -37 percent	{ +65 percent -37 percent	{ +104 percent -37 percent
Offset	{ +44 percent -33 percent		
Afterbody	{ +88 percent -53 percent		

These final maximum deviations are indicated for the Flight 1 results in figure 10.

EFFECTS OF BODY MOTIONS ON STAGNATION HEATING RATES

The influence of the body motions on the results obtained during the second data period is referred to several times in this report. A detailed analysis of these motions is presented in reference 35. In order to make a reasonable estimate of these influences, a relationship which can be used to adjust the Fire heating rates to values representative of zero-angle-of-attack values was established.

It was necessary to determine, initially, the effects of angle of attack on the measured radiation at the geometrical stagnation point. Figure 8 shows the variation of the parameter $\left(\frac{\dot{q}_{R,\alpha}}{\dot{q}_{R,\alpha=0}} \right)_{s/s_c=0}$ with angle of attack for bodies of varying bluntness. The uppermost curve for $R_n/D = 1.42$ (bluntness of first phenolic-asbestos heat shield) was deduced from the Flight 1 data as follows:

(a) A smooth curve was faired across the peaks of the stagnation radiometer record during the time that this particular shield was exposed.

(b) From the angle-of-attack history during that same period, it was observed that the minimum angle of attack was periodically and consistently 5.5° . (See fig. 7 during the elapsed time around 1668 sec.) The records indicated that the peak radiometer values in its oscillatory pattern were in phase with these periodic minimums in the angle-of-attack history. On this basis, it was assumed that the peaks in the stagnation radiometer records were manifesting themselves at $\alpha = 5.5^\circ$.

(c) If the theoretical curves of figure 8 for the less blunt bodies ($r_n/D = 1.0$ and 1.2) are used as a guide, a value of the parameter

$\left(\frac{\dot{q}_{R,\alpha}}{\dot{q}_{R,\alpha=0}} \right)_{s/s_c=0}$ was assumed for r_n/D at $\alpha = 5.5^\circ$. On the basis of this

assumption, the faired curve across the peaks of the oscillations of the radiometer record was raised to correspond to the "adjusted" zero angle-of-attack condition.

(d) A time history of the parameter $\left(\frac{\dot{q}_{R,\alpha}}{\dot{q}_{R,\alpha=0}} \right)_{s/s_c=0}$ was obtained by

dividing the values from the radiometer record to the "adjusted" fairing for the zero angle-of-attack condition. The points shown in figure 8 are actual values that resulted from this calculation.

(e) A curve was faired through the resulting points on figure 8 with

$$\left(\frac{\dot{q}_{R,\alpha}}{\dot{q}_{R,\alpha=0}} \right)_{s/s_c=0} = 1.0 \text{ at } \alpha = 0^\circ \text{ used as an end point. The location of the}$$

point corresponding to the assumed value of the parameter at $\alpha = 5.5^\circ$ (step (c)) was used to assess the accuracy of that initial assumption. If the assumed value of the parameter at $\alpha = 5.5^\circ$ did not fall on the faired curve through the remaining points, a new value was assumed and the calculations

repeated. After two iterations, a value of $\left(\frac{\dot{q}_{R,\alpha}}{\dot{q}_{R,\alpha=0}} \right)_{s/s_c=0}$ of 0.94 produced

a satisfactory curve.

A similar factor to account for angle-of-attack effects on convective heating was deduced from reference 36.

As a first step in adjusting calorimeter fluxes for angle-of-attack deviations, the basic equation to allow separately for the effects of radiative and convective heating was then written as follows:

$$(\dot{q}_C + \alpha_{Be} \dot{q}_R) \bar{F}_e = F_C \dot{q}_C + F_R \alpha_{Be} \dot{q}_R \quad (B1)$$

where

$$\alpha_{Be} = \frac{\int_0^\infty I_{o,\lambda} \alpha_{Be,\lambda} d\lambda}{\int_0^\infty I_{o,\lambda} d\lambda} \quad (B2)$$

$$F_C = \frac{\int_{t_i}^{t_f} \left(\frac{\dot{q}_{C,\alpha}}{\dot{q}_{C,\alpha=0}} \right)_{s/s_c=0} dt}{t_f - t_i} \quad (B3)$$

$$F_R = \frac{\int_{t_i}^{t_f} \left(\frac{\dot{q}_{R,\alpha}}{\dot{q}_{R,\alpha=0}} \right)_{s/s_c=0} dt}{t_f - t_i} \quad (B4)$$

and \bar{F}_e is the factor by which to adjust the calorimeter stagnation total heating rates to account for body motions. Theoretical values of $I_{0,\lambda}$, \dot{q}_C , and \dot{q}_R were used in equations (B1) to (B4). The time span of the second data period, $t_f - t_i$, was approximately 3.5 sec for the calorimeter experiment. During this time the body motions were calculated to have occurred at a frequency of approximately 7 cps as indicated by the angle-of-attack history shown in figure 5. Considering the instantaneous heating rates deduced from the calorimeter data for the second data period (ref. 10) to be essentially the mean of those for any angle of attack within the envelope shown in figure 7, the angle between the coning axis and flight path (shown as the median line in fig. 7) was assumed to be representative of the effective angle of attack during that time period. With the use of these inputs, values of F_R and F_C were then deduced for the second data period.

Self-absorption of radiation in the gas cap was assumed to apply in the vacuum ultraviolet wavelength range from 0.04μ to 0.113μ . Atomic line radiation was deduced from reference 25. The general form of equation (B1) was modified therefore to accurately account for the various radiative contributions. The factor \bar{F}_e by which the calorimeter data were finally adjusted was therefore calculated from the following relationship:

$$\bar{F}_e = \frac{\dot{q}_C F_C + \left[(\alpha_{Be} \dot{q}_{vuv})_{0.04 < \lambda < 0.113} + (\alpha_{Be} \dot{q}_t)_{0.116 < \lambda < 2.0} + (\alpha_{Be} \dot{q}_{al})_{\lambda > 0.2} + (\alpha_{Be} \dot{q}_{al})_{\lambda < 0.2} \right] F_R}{\dot{q}_C + (\alpha_{Be} \dot{q}_{vuv})_{0.04 < \lambda < 0.113} + (\alpha_{Be} \dot{q}_t)_{0.116 < \lambda < 2.0} + (\alpha_{Be} \dot{q}_{al})_{\lambda > 0.2} + (\alpha_{Be} \dot{q}_{al})_{\lambda < 0.2}} \quad (B5)$$

The value of \dot{q}_{vuv} represents the incident radiation at the body surface at the low vacuum-ultraviolet wavelengths calculated from reference 24.

The following table indicates the values that were used in solving equation (B5) and the subsequent results of \bar{F}_e by which the basic Fire calorimeter data at stagnation were adjusted:

t , sec	\dot{q}_C , W/cm ²	F_C	α_{Be} ($0.04 \mu < \lambda < 0.113 \mu$)	\dot{q}_{vuv}	α_{Be} ($0.116 \mu < \lambda < 2.0 \mu$)	\dot{q}_t	\dot{q}_{al} ($\lambda > 0.2 \mu$)	$(\alpha_{Be})_{al}$ ($\lambda > 0.2 \mu$)	\dot{q}_{al} ($\lambda < 0.2 \mu$)	$(\alpha_{Be})_{al}$ ($\lambda < 0.2 \mu$)	F_R	\bar{F}_e
1671	564	0.855	0.95	283	0.545	180	345	0.51	379	0.67	0.788	0.815
1672	604	.864	.95	317	.545	245	477	.51	481	.67	.793	.820
1673	636	.872	.95	292	.545	286	581	.51	498	.67	.797	.825

[REDACTED]

APPENDIX C

RADIATION CALCULATIONS

The purpose of this appendix is to outline the procedure used to predict the levels of stagnation radiation experienced by a blunt body during a given reentry. The necessary inputs to the calculation are the reentry trajectory, that is, time histories of altitude and velocity; the local atmosphere in the reentry area, that is, ambient conditions of pressure and density with altitude; and reentry vehicle shape and size.

For the purposes of this report, the equilibrium radiation values deduced from the absorption coefficients of reference 5 and the nonequilibrium levels based on the methods of reference 1 were used. Data presented in reference 6 are also used to supplement the information for the nonequilibrium estimates.

Determination of Characteristic Dimensions

of Radiation Intensity Profile

In estimating the stagnation radiative heating for Flight 1, the equilibrium and nonequilibrium radiation zones (fig. 11) are considered separately. In order to estimate with reasonable accuracy the contribution from the equilibrium zone which is dependent upon its thickness, the shock standoff distance δ_{ne} and the relaxation distance $d_{0.1}$ must be determined. If truncation, a nonequilibrium radiation-limiting phenomenon discussed earlier, is evident, the excitation distance d_p is also necessary for estimating the radiation to the reentering body under these conditions.

Calculations of $d_{0.1}$ and d_p . - Data on relaxation and excitation distances for one-dimensional shock-tube flow are presented in reference 6. In that report, these distances were determined in terms of laboratory reference times $t_{0.1,lab}$ and $t_{p,lab}$. These are functions of the shock velocity U_s and the laboratory measuring technique that was used. In order to make these laboratory times useful, they must first of all be converted to residence times $t_{0.1,res}$ and $t_{p,res}$ by considering the velocity distribution in the shocked gas. The residence time for relaxation $t_{0.1,res}$ is defined as the time a particle traveling in the flow behind the shock takes to relax to chemical equilibrium. An analogous approach in terms of average particle velocity may be used to define the excitation time in the flow $t_{p,res}$. This initial conversion from the laboratory reference values may be expressed as

$$d_{0.1,lab} = U_s t_{0.1,lab} = (V_{2,0.1})_{av} t_{0.1,res} \quad (C1)$$

and

$$d_{p,lab} = U_{stp,lab} = (V_{2,p})_{av} t_{p,res} \quad (C2)$$

Equations (C1) and (C2) are solved for $t_{0.1,res}$ and $t_{p,res}$, respectively. In these equations, the average flow velocities $(V_{2,0.1})_{av}$ and $(V_{2,p})_{av}$ represent estimates of the average flow velocity behind a normal shock for the case of one-dimensional shock-tube flow. The velocity functions

$$(V_{2,0.1})_{av} = \frac{\frac{1}{6} U_s + \frac{\rho_1}{\rho_2} U_s}{2} \quad (C3)$$

and

$$(V_{2,p})_{av} = \frac{\frac{1}{6} U_s + \frac{1}{9} U_s}{2} \quad (C4)$$

are simplified linear versions of the distributions suggested in reference 1.

For the flight case, it is assumed that the one-dimensional nonequilibrium zone model can be applied to streamline flow in the shock layer by matching the excitation times and relaxation times of the one-dimensional case which was just considered, that is,

$$t_{0.1} = t_{0.1,res} \quad (C5)$$

and

$$t_p = t_{p,res} \quad (C6)$$

where $t_{0.1}$ and t_p are, respectively, the relaxation and excitation times for the flight case. The flight velocity V_∞ is substituted for the shock velocity U_s in applying equations (C1) to (C4) for the flight case calculation. The velocity distribution along the stagnation streamline for one particular nonequilibrium flow condition was deduced from the flow-field study of reference 21, which included a calculation of the flow field surrounding the Fire reentry package for an early reentry condition (see actual conditions in body of this report). The mass continuity principle was applied to the calculated density variation along that streamline and the resulting velocity profile

APPENDIX C

yielded values of $[(v_{2,0.1})_{av}]_{\text{Fire}}$ and $[(v_{2,p})_{av}]_{\text{Fire}}$ that can be approximated in the stagnation region between the shock and the body by the expressions

$$[(v_{2,0.1})_{av}]_{\text{Fire}} = (0.138 - 0.00355d_{0.1})v_{\infty} \quad (C7)$$

$$[(v_{2,p})_{av}]_{\text{Fire}} = (0.138 - 0.00355d_p)v_{\infty} \quad (C8)$$

Substituting $d_{0.1}/t_{0.1}$ for $[(v_{2,0.1})_{av}]_{\text{Fire}}$ and d_p/t_p for $[(v_{2,p})_{av}]_{\text{Fire}}$, the relaxation and excitation distances for the flight case may be expressed as:

$$d_{0.1} = \frac{0.0138v_{\infty}t_{0.1}}{1 + 0.000355v_{\infty}t_{0.1}} \quad (C9)$$

$$d_p = \frac{0.0138v_{\infty}t_p}{1 + 0.000355v_{\infty}t_p} \quad (C10)$$

where $d_{0.1}$ and d_p are in units of cm, v_{∞} in km/sec or mm/ μ sec, and $t_{0.1}$ and t_p in μ sec. For the condition of nonequilibrium flow investigated in reference 21, $d_{0.1}$ and d_p were calculated by equations (C9) and (C10) to be 5.24 and 2.11 cm, respectively.

These calculations were made for one particular high-altitude low-density condition based on a preflight trajectory and the 1962 U.S. Standard Atmosphere (ref. 29). The shock properties and shock characteristics for Project Fire can be very nearly approximated by matching the ambient density for equilibrium and nonequilibrium flow conditions; the effect of the difference in velocity for the two calculations was not significant in this instance. The Flight 1 conditions used to approximate those of reference 21 were $h = 78.6$ km (257 720 ft), $v_{\infty} = 11.6$ km/sec (38 013 fps), $\rho_1/\rho_0 = 1.928 \times 10^{-5}$ at $t \approx 1662.8$ sec. Figure 16 of reference 6 indicates equations of the form

$$(d_{0.1})^{K_1} \left(\frac{\rho_1}{\rho_0} \right) = B_1 \quad (C11)$$

and

APPENDIX C

$$(d_p)^{K_2} \left(\frac{\rho_1}{\rho_0} \right) = B_2 \quad (C12)$$

relating the relaxation and excitation distances with ambient density conditions for the one-dimensional shock-tube case (K_1 and $K_2 = 1$ for constant shock velocity in ref. 6). Equations of this form were assumed to apply in establishing relationships for $d_{0.1}$ and d_p as functions of ambient density for the Fire reentry case. Although the flight velocity was changing in the Fire trajectory, the change is minimal during the early reentry times characterized by strong nonequilibrium contributions where $d_{0.1}$ and d_p are most influential in determining radiation levels. The values of $d_{0.1}$ and d_p obtained in equations (C9) and (C10) were used as the high-altitude boundary conditions for the determination of the constants B_1 , K_1 , B_2 , and K_2 in equations (C11) and (C12) for the Fire reentry trajectory; the ambient density for the Fire reentry was matched with that of the flow-field calculation at this nonequilibrium boundary point.

The second flight boundary condition was assumed to be one characterized by almost strictly equilibrium flow. At an altitude of 45.7 km (150 000 ft) at $t \approx 1675.8$ sec and an ambient density ratio ρ_1/ρ_0 equal to 1.392×10^{-3} , the flight velocity was approximately 9.75 km/sec (32 000 ft/sec) and $d_{0.1}$ and d_p were calculated to be 0.12 cm and 0.042 cm, respectively, by using the equations

$$d_{0.1} = t_{0.1,lab} V_\infty \quad (C13)$$

$$d_p = t_{p,lab} V_\infty \quad (C14)$$

These equations may be deduced directly from equations (C1) and (C2) if it is assumed that the velocity profile behind the shock to the relaxation point in the equilibrium flight case is approximately the same as that for one-dimensional shock-tube case. The resulting relationships for $d_{0.1}$ and d_p for the Flight 1 trajectory were

$$d_{0.1} = \left[\frac{1.254 \times 10^{-4}}{(\rho_1/\rho_0)_{\text{Fire}}} \right]^{0.885} \quad (C15)$$

and

$$d_p = \left[\frac{4.362 \times 10^{-5}}{(\rho_1/\rho_0)_{\text{Fire}}} \right]^{0.915} \quad (C16)$$

APPENDIX C

Calculation of δ_{ne} . - As was indicated in the body of the report (eq. (7)), the relationship that was used in the Flight 1 calculations to approximate the equilibrium shock standoff distance was

$$\delta_e = \frac{3}{4} \frac{\rho_1}{\rho_2} r_n$$

It can be seen from mass continuity considerations that if the gas behind the shock along the stagnation streamline remains in a nonequilibrium state for any extended period of time, the average density of that shocked gas is less than that for equilibrium flow and the shock must stand off a greater distance from the body. The method of Katzen and Kaattari (ref. 37) was used to estimate the shock standoff distance which includes the nonequilibrium effects. That method is based on the continuity principle and an exponential density profile in the shocked gas. The average gas density between the shock and the wall is given by the expression

$$\frac{\bar{\rho}_{ne}}{\rho_\infty} = \frac{\rho_{fr}}{\rho_\infty} \left\{ \frac{\sqrt{\left(\frac{\delta_{fr} K}{V_\infty} \frac{\rho_{fr}}{\rho_\infty} - 1 \right)^2 + 4 \frac{\rho_2}{\rho_\infty} \frac{\delta_{fr} K}{V_\infty} - \left(\frac{\delta_{fr} K}{V_\infty} \frac{\rho_{fr}}{\rho_\infty} - 1 \right)}}{2} \right\} \quad (C17)$$

where

$$K = 1.29 \times 10^{-14} (\rho_\infty / \rho_o) V_\infty^6 \quad (C18)$$

$$\frac{\rho_{fr}}{\rho_\infty} = 5.97 \quad \text{(assumed to remain constant over Mach number range experienced in Fire reentry)}$$

$$\delta_{fr} = \frac{3}{4} \frac{\rho_\infty}{\rho_{fr}} r_n \quad (C19)$$

In this system of equations, the flight velocity V_∞ is in units of m/sec; δ and r_n are in m. The final value of the stagnation shock standoff distance adjusted for nonequilibrium effects, is given by

$$\delta_{ne} = \frac{3}{4} \frac{\rho_\infty}{\rho_{ne}} r_n \quad (C20)$$

APPENDIX C

Calculation of Nonequilibrium Radiation

The base value of the nonequilibrium radiative heating rate $\dot{q}_{ne,P}$ for the Fire reentry package was obtained directly from figure 18 of reference 1. Base value means the level of radiation that has not been adjusted for radiation-limiting phenomena or shock geometry. The truncation correction, if applicable, was applied by approximating the stagnation streamline by a straight line from the shock to the body. The nonequilibrium radiation intensity profile illustrated in figure 11 was approximated by a triangle, and basic geometrical relations were used to deduce the heating contribution from the untruncated portion of the nonequilibrium zone. A correction factor equal to 0.84 (deduced from ref. 14) was also applied to the base values of reference 1 to account for shock geometry effects resulting from the particular bluntness of the Fire vehicle. For conditions where truncation was not a factor, the nonequilibrium radiative heating rate for the stagnation region was given by

$$\dot{q}_{ne} = 0.84 \dot{q}_{ne,P} \quad (C21)$$

In equation form, the truncated nonequilibrium radiative heating rate is approximated by

$$(\dot{q}_{ne,P})_{trunc} = 0.84 \frac{A_{trunc}}{A} \dot{q}_{ne,P} \quad (C22)$$

The collision-limiting effect was assumed to apply to both the nonequilibrium and equilibrium radiation and is discussed in the section "Calculation of Collision Limiting."

Calculation of Equilibrium Radiation

Equilibrium stagnation radiative heating is a function of temperature and density in the shocked gas and the shock standoff distance; these in turn are dependent upon flight and atmospheric conditions and body shape. Equilibrium radiation (refs. 3, 4, 5, and 7) is generally presented, however, as a function of the two gas properties, temperature and density. The length of the equilibrium zone, equal to the shock standoff distance δ_{ne} less the relaxation distance $d_{0.1}$ may be determined from the section "Determination of Characteristic Dimensions of Radiation Intensity Profile." The equilibrium gas temperature T_2 and density $\frac{\rho_2}{\rho_{ref}}$ may be extracted directly from shock tables, but, for this report, the values were obtained from an inhouse program in which the thermodynamic properties of reference 38 were tabulated. The conservation equations of mass, momentum, and energy and the equation of state were solved across a

APPENDIX C

normal shock applying the necessary iteration on $\frac{\rho_2}{\rho_{ref}}$ (1 percent accuracy) to arrive at the values of the various shock properties.

The absorption coefficients of reference 5 were inserted into a radiation program and values of $\dot{q}_{R,M}/l$ for $l = 1$ cm were determined for the Fire trajectory. These values were then multiplied by the equilibrium zone length $\delta_{ne} - d_{0.1}$ to obtain the contribution from equilibrium radiation. A shock shape factor of 0.84 was used in determining the final values of equilibrium stagnation heating for the Fire body. The relationship for the equilibrium radiation intensity is

$$\frac{q_{R,M}}{l} = 4\pi(0.84) \sum \frac{\mu_{\lambda} \hbar c^2}{\lambda^5 [\exp(\hbar c / \lambda k T) - 1]} \Delta\lambda \quad (C23)$$

Calculations were made for the radiation over the wavelength range from 0.1167 μ to 1.9837 μ . A separate analysis was also made for $\dot{q}_{R,M}/l$ for the wavelength range more nearly associated with Project Fire - namely, from 0.23 μ to 1.9837 μ . The results for both wavelength ranges are indicated in figure 10.

The value of equilibrium radiation was then obtained by

$$\dot{q}_e = \frac{\dot{q}_{R,M}}{l} \times (\delta_{ne} - d_{0.1}) \quad (C24)$$

The value of \dot{q}_e was then added to that for nonequilibrium obtained from reference 1.

$$\dot{q}_t^* = \dot{q}_e + \dot{q}_{ne} \quad (C25)$$

This estimate of radiative heating does not consider contributions from atomic line radiation.

Calculation of Collision Limiting

A factor to account for the effect of collision limiting was applied to the total radiation which consisted of both the equilibrium and nonequilibrium contributions. The final predicted stagnation radiative heating values (excluding the vacuum ultraviolet) were determined from

$$\dot{q}_t = F_{cl} \dot{q}_t^* \quad (C26)$$

where F_{cl} is the collision-limiting factor based on reference 6 and indicated in figure 12.

[REDACTED]

REFERENCES

1. Page, William A.; and Arnold, James O.: Shock-Layer Radiation of Blunt Bodies at Reentry Velocities. NASA TR R-193, 1964.
2. Page, William A.; Canning, Thomas N.; Craig, Roger A.; and Stephenson, Jack D.: Measurements of Thermal Radiation of Air From the Stagnation Region of Blunt Bodies Traveling at Velocities up to 31,000 Feet Per Second. NASA TM X-508, 1961.
3. Kivel, B.; and Bailey, K.: Tables of Radiation From High Temperature Air. Res. Rept. 21 (Contracts AF 04(645)-18 and 49(638)-61), AVCO Res. Lab., Dec. 1957.
4. Nardone, M. C.; Breene, R. G.; Zeldin, S. S.; and Riethof, T. R.: Radiance of Species in High Temperature Air. Tech. Inform. Ser. R63SD3 (Contract AF 04(694)-222), Missile and Space Div., Gen. Elec. Co., June 1963. (Available from DDC as AD No. 408564.)
5. Meyerott, R. E.; Sokoloff, J.; and Nicholls, R. A.: Absorption Coefficients of Air. AFRCR-TR-59-296, U.S. Air Force, Sept. 1959.
6. Allen, R. A.; Rose, P. H.; and Camm, J. C.: Non-Equilibrium and Equilibrium Radiation at Super-Satellite Re-Entry Velocities. Paper No. 63-77, Inst. Aerospace Sci., Jan. 1963.
7. Nerem, Robert M.; and Stickford, George H.: Shock Layer Radiation During Hypervelocity Re-Entry. AIAA Entry Technology Conference, CP-9, Am. Inst. Aeron. Astronaut., Oct. 1964, pp. 158-169.
8. SLV Test Evaluation and Guidance Software Groups: Project Fire Integrated Post Flight Evaluation Report - Flight No. 1. GDA/BKF-64-018 (NASA CR-57017), Gen. Dyn./Astronaut., Oct. 30, 1964.
9. Dingeldein, Richard C.: Flight Measurements of Reentry Heating at Hyperbolic Velocity (Project Fire). NASA TM X-1053, 1965.
10. Cornette, Elden S.: Forebody Temperatures and Total Heating Rates Measured During Project Fire 1 Reentry at 38 000 Feet Per Second. NASA TM X-1120, 1965.
11. Slocumb, Travis H., Jr.: Project Fire Flight 1 Heating and Pressure Measurements on the Reentry-Vehicle Afterbody at a Velocity of 38 000 Feet Per Second. NASA TM X-1178, 1965.
12. Goldsmith, Alexander; Hirschhorn, Harry J.; and Waterman, Thomas E.: Thermophysical Properties of Solid Materials. Volumn III - Ceramics. WADC Tech. Rept. 58-476, Vol. III, U.S. Air Force, Nov. 1960. (Available from ASTIA as AD No. 265597.)

13. McMahon, H. O.: Thermal Radiation From Partially Transparent Reflecting Bodies. J. Opt. Soc. Am., vol. 40, no. 6, June 1950, pp. 376-380.
14. Bobbitt, Percy J.: Effects of Shape on Total Radiative and Convective Heat Inputs at Hyperbolic Entry Speeds. Vol. 13 of Advances in Astronautical Sciences, Eric Burgess, ed., Western Periodicals Co. (N. Hollywood, Calif.), c.1963, pp. 290-319.
15. McAdams, William H.: Heat Transmission. Third Ed., McGraw-Hill Book Co., Inc., 1954.
16. Scallion, William I.; and Lewis, John H., Jr.: Flight Parameters and Vehicle Performance for Project Fire Flight 1, Launched April 14, 1964. NASA TN D-2996, 1965.
17. Wick, Bradford H.: Radiative Heating of Vehicles Entering the Earth's Atmosphere. The High Temperature Aspects of Hypersonic Flow, Wilbur C. Nelson, ed., AGARDograph 68, The Macmillan Co., 1964, pp. 607-627.
18. Stainback, P. Calvin: Convective and Equilibrium Radiation Heat-Transfer Predictions for Project Fire Reentry Vehicle. NASA TN D-2867, 1965.
19. Vinokur, M; Nicolet, W. E.; Buckingham, A. C.; and Hoshizaki, H.: Project Fire - Flow Field Prediction and Analysis. M-12-65-1 (NASA CR-63401), Lockheed Missiles & Space Co., Mar. 1965.
20. Brunner, M. J.; Dohner, C. V.; Langelo, V. A.; and Rie, H.: Flow Field Prediction and Analysis - Project Fire. Doc. No. 64SD727 (NASA CR-60451), Re-Entry Syst. Dept., Gen. Elec. Co., May 29, 1964.
21. Kuby, W. C.; Byron, S. R.; Foster, R. M.; Hoglund, R. F.; and Holt, M.: Analysis of the Project Fire Re-Entry Package Flow Field. Publ. No. U-3020 (NASA CR-63388), Aeronutronic Div., Philco Corp., Oct. 8, 1964.
22. Kivel, Bennett: Chemistry, Ionization and Radiation in the Non-Equilibrium Front of Normal Shocks in Air. AMP 34 (Contract Nos. AF 04(647)-278 and DA-19-020-ORD-4862), Avco-Everett Res. Lab., Sept. 1959.
23. Camm, J. C.; Kivel, B.; Taylor, R. L.; and Teare, J. D.: Absolute Intensity of Non-Equilibrium Radiation in Air and Stagnation Heating at High Altitudes. J. Quant. Spectry. & Radiative Transfer, vol. 1, no. 1, Sept. 1961, pp. 53-75.
24. Hahne, Gerhard E.: The Vacuum Ultraviolet Radiation From N^+ and O^+ -Electron Recombination in High-Temperature Air. NASA TN D-2794, 1965.
25. Allen, Richard A.: Air Radiation Graphs: Spectrally Integrated Fluxes Including Line Contributions and Self Absorption. Res. Rept. 230 (Contract Nos. NASw-748 and DA-01-021-AMC-12005(2)), Avco-Everett Res. Lab., Sept. 1965.

- [REDACTED]
26. Biberman, L. M.; and Norman, G. E.: On the Calculation of Photoionization Absorption. Opt. Spectry. (USSR), vol. viii, no. 4, Apr. 1960, pp. 230-232.
 27. Boldt, G.: Rekombinations- und "Minus"-Kontinuum der Stickstoffatome. Z. Physik, Bd. 154, Heft 1959, pp. 330-338.
 28. Allen, R. A.; and Textoris, A.: New Measurements and a New Interpretation for High Temperature Air Radiation. Preprint No. 64-72. Am. Inst. Aeron. Astronaut., Jan. 1964.
 29. Anon.: U.S. Standard Atmosphere, 1962: NASA, U.S. Air Force, and U.S. Weather Bur., Dec. 1962.
 30. Breene, R. G., Jr.; and Nardone, Maria: Radiation Emission From High Temperature Equilibrium Air. R61SD020 (Contract No. AF04(647)269), Space Sci. Lab., Gen. Elec. Co., May 1961.
 31. Kaattari, George E.: Predicted Shock Envelopes About Two Types of Vehicles at Large Angles of Attack. NASA TN D-860, 1961.
 32. Hoshizaki, H.: Equilibrium Total Radiation Measurements in Air at Super-orbital Entry Velocities. Third Hypervelocity Techniques Symposium. Univ. of Denver and Arnold Eng. Develop. Center, Mar. 1964, pp. 245-281.
 33. Hoshizaki, Hiroshi: Shock Tube Emission Coefficient Measurements in Air. 6-75-65-4, Lockheed Missiles & Space Co.
 34. Cohen, Nathaniel B.: Boundary-Layer Similar Solutions and Correlation Equations for Laminar Heat-Transfer Distribution in Equilibrium Air at Velocities up to 41,000 Feet Per Second. NASA TR R-118, 1961.
 35. Woodbury, Gerard E.: Angle-of-Attack Analysis for Project Fire 1 Payload Reentry Flight. NASA TN D-3366, 1966.
 36. Jones, Robert A.: Measured Heat-Transfer and Pressure Distributions on the Apollo Face at a Mach Number of 8 and Estimates for Flight Conditions. NASA TM X-919, 1964.
 37. Katzen, Elliott D.; and Kaattari, George E.: Inviscid Hypersonic Flow Around Blunt Bodies. AIAA J., vol. 3, no. 7, July 1965, pp. 1230-1237.
 38. Hilsenrath, Joseph; Klein, Max; and Woolley, Harold W.: Tables of Thermodynamic Properties of Air Including Dissociation and Ionization from 1,500° K to 15,000° K. AEDC-TR-59-20, U.S. Air Force, Dec. 1959. (Available from ASTIA as AD 229934.)

TABLE I.- FLIGHT 1 PARAMETERS AND SUMMARY OF CALCULATED VALUES

(1) t, sec	(2) h		(3) V _∞		(4) $(\rho_1/\rho_0)_{\text{Fire}}$	(5) $\log \frac{\rho_2}{\rho_{\text{ref}}}$	(6) T ₂ , °K	(7) ρ_1/ρ_2	(8) δ_{ne} , cm	(9) $d_{0.1}$, cm	(10) $\delta_{\text{ne}} - d_{0.1}$, cm
	km	ft	km/sec	fps							
1658	91.773	301 093	11.60	38 045	2.000 × 10 ⁻⁶	-4.412	9 355	4.692 × 10 ⁻²	4.62	39.002	Trunc
1659	89.006	292 016	11.60	38 048	3.166 × 10 ⁻⁶	-4.257	9 510	5.202 × 10 ⁻²	4.59	25.967	Trunc
1660	86.252	282 978	11.60	38 048	5.062 × 10 ⁻⁶	-4.063	9 704	5.324 × 10 ⁻²	4.38	17.139	Trunc
1661	83.509	273 980	11.60	38 044	7.221 × 10 ⁻⁶	-3.915	9 860	5.395 × 10 ⁻²	4.27	12.516	Trunc
1662	80.779	265 022	11.59	38 032	1.144 × 10 ⁻⁵	-3.720	10 073	5.458 × 10 ⁻²	4.15	8.326	Trunc
1663	78.062	256 109	11.59	38 009	2.160 × 10 ⁻⁵	-3.453	10 392	5.574 × 10 ⁻²	4.09	4.745	Trunc
1664	75.360	247 243	11.57	37 969	3.234 × 10 ⁻⁵	-3.285	10 603	5.664 × 10 ⁻²	4.09	3.319	0.77
1665	72.673	238 428	11.55	37 907	4.764 × 10 ⁻⁵	-3.123	10 835	5.752 × 10 ⁻²	4.12	2.355	1.76
1666	70.003	229 668	11.53	37 830	7.060 × 10 ⁻⁵	-2.959	11 103	5.842 × 10 ⁻²	4.15	1.663	2.49
1667	67.351	220 968	11.50	37 717	1.070 × 10 ⁻⁴	-2.786	11 357	5.938 × 10 ⁻²	4.20	1.151	3.05
1668	64.721	212 338	11.45	37 554	1.473 × 10 ⁻⁴	-2.654	11 429	6.040 × 10 ⁻²	4.26	.867	3.40
1669	62.115	203 791	11.38	37 329	2.339 × 10 ⁻⁴	-2.464	11 548	6.191 × 10 ⁻²	4.36	.576	3.78
1670	59.540	195 341	11.28	37 019	3.114 × 10 ⁻⁴	-2.347	11 602	6.296 × 10 ⁻²	4.43	.447	3.98
1671	59.540	195 341	11.28	37 019	3.114 × 10 ⁻⁴	-2.347	11 602	6.296 × 10 ⁻²	3.82	0.447	3.37
1672	57.000	187 009	11.16	36 598	3.990 × 10 ⁻⁴	-2.245	11 623	6.372 × 10 ⁻²	3.86	.359	3.50
1673	54.506	178 824	10.98	36 035	5.293 × 10 ⁻⁴	-2.125	11 608	6.423 × 10 ⁻²	3.89	.279	3.61
1674	52.065	170 816	10.76	35 301	7.044 × 10 ⁻⁴	-2.007	11 444	6.514 × 10 ⁻²	3.94	.217	3.72
1675	49.690	163 025	10.47	34 352	9.323 × 10 ⁻⁴	-1.890	11 189	6.577 × 10 ⁻²	3.98	.169	3.81
1676	47.397	155 502	10.10	33 146	1.217 × 10 ⁻³	-1.777	10 717	6.616 × 10 ⁻²	4.00	.134	3.86
1677	45.203	148 303	9.64	31 641	1.597 × 10 ⁻³	-1.655	9 839	6.556 × 10 ⁻²	3.96	.105	3.86
1677	43.127	141 492	9.08	29 802	2.115 × 10 ⁻³	-1.516	8 829	6.304 × 10 ⁻²	3.81	.082	3.73
1677	43.127	141 492	9.08	29 802	2.115 × 10 ⁻³	-1.516	8 829	6.304 × 10 ⁻²	3.33	0.082	3.24
1678	41.190	135 139	8.43	27 648	2.701 × 10 ⁻³	-1.408	8 079	6.286 × 10 ⁻²	3.32	.066	3.25
1679	39.410	129 298	7.69	25 238	3.441 × 10 ⁻³	-1.317	7 570	6.497 × 10 ⁻²	3.43	.053	3.38
1680	37.798	124 010	6.91	22 667	4.344 × 10 ⁻³	-1.245	7 131	6.947 × 10 ⁻²	3.67	.043	3.63
1681	36.360	119 292	6.12	20 065	5.241 × 10 ⁻³	-1.206	6 648	7.655 × 10 ⁻²	4.05	.037	4.01
1682	35.092	115 132	5.35	17 555	6.310 × 10 ⁻³	-1.172	6 084	8.532 × 10 ⁻²	4.52	.031	4.48
1683	33.983	111 494	4.65	15 243	7.500 × 10 ⁻³	-1.133	5 218	9.272 × 10 ⁻²	4.92	.027	4.89
1684	33.017	108 324	4.02	13 188	8.647 × 10 ⁻³	-1.085	4 215	9.566 × 10 ⁻²	5.10	.024	5.07
1685	32.176	105 564	3.48	11 404	9.715 × 10 ⁻³	-1.057	3 589	1.008 × 10 ⁻¹	5.41	.021	5.39

TABLE I.- FLIGHT I: PARAMETER AND SUMMARY OF CALCULATED VALUES - Continued

(1) τ , sec	(2) \dot{q}_p , cm	(3) \dot{q}_e , W/cm ² (ref. 1)	(4) \dot{q}_e , W/cm ² (0.115 < λ < 2.0) (ref. 5)	(5) \dot{q}_e , W/cm ² (0.20 < λ < 10) (ref. 3)	(6) \dot{q}_e , W/cm ² (0.20 < λ < 10) (ref. 4)	(7) \dot{q}_e , W/cm ² (0.20 < λ < 10) (ref. 7)	(8) \dot{q}_e , W/cm ² (λ > 0.2) (ref. 25)	(9) \dot{q}_e , W/cm ² (λ < 0.2) (ref. 25)	(10) $\dot{q}_{e,av}$, W/cm ² (0.04 < λ < 0.2-3) (ref. 24)
1558	16.886	0.53							
1559	11.069	1.20							
1560	7.199	2.56							
1561	5.199	4.58							
1562	3.409	9.38							
1563	1.305	15.8							
1564	1.315	15.2	0.26	2.22	1.17	0.41	2.23	6.11	
1565	1.922	16.1	1.63	12.5	5.19	1.95	9.55	20.6	
1566	2.43	16.0	6.51	39.4	15.0	5.94	26.1	46.5	
1567	3.39	15.8	21.4	94.2	40.0	15.5	60.7	90.7	
1568	3.28	15.6	-0.4	157	71.3	27.2	100	133	93.0
1569	2.14	15.2	89.1	321	159	59.9	200	233	134
1570	1.17	14.7	139	483	251	94.1	297	322	210
1571	0.165	14.7							262
1572	1.131	14.1	117	408	213	79.6	252	295	244
1573	1.078	13.2	166	565	307	114	345	379	283
1574	0.60	11.0	232	785	447	165	477	481	317
1575	0.7	9.56	274	982	554	203	581	498	292
1576	0.37	7.97	290	982	570	230	615	456	236
1577	0.029	6.31	244	790	439	196	473	317	138
			144	390	201	100	195	124	42.6
			79.6	158	77.5	41.9	45.8	25.9	7.63
1677	0.029	6.31	69.2	138	67.4	36.4	39.9	23.9	7.24
1678	0.023	4.71	45.3	71.8	34.2	19.7	11.2	5.63	1.46
1679	0.018	3.30	30.3	28.6	23.4	14.8	4.05	1.70	
1680	0.015	2.17	22.6	20.6	17.3	12.0	1.67	.60	
1681	0.012	1.35	15.4	13.7					
1682	0.010	.80	9.59	8.28					
1683	0.009	.46	3.87	3.18					
1684	0.008	.26	.83	.69					
1685	0.007	.15	.11	.10					

TABLE I.- FLIGHT 1 PARAMETERS AND SUMMARY OF CALCULATED VALUES - Concluded

[illegible]

Beryllium layer	D, m	r_n , m	r_c , m
1	0.672	0.935	0.010
2	.630	.805	.036
3	.587	.702	.006

Sensor locations

- Radiometer
 + Thermocouples
 Δ Static pressure transducer

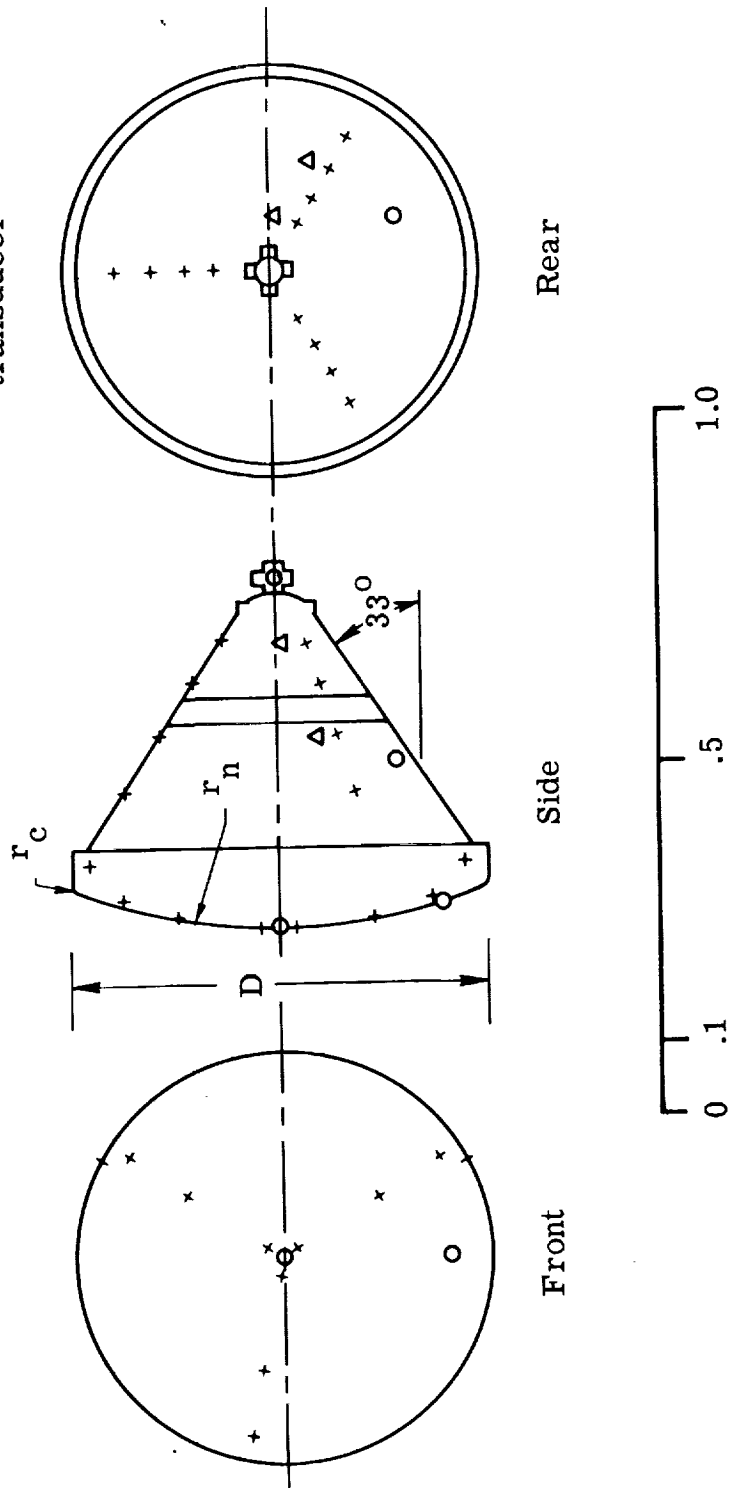


Figure 1.- Reentry package geometry and sensor locations.

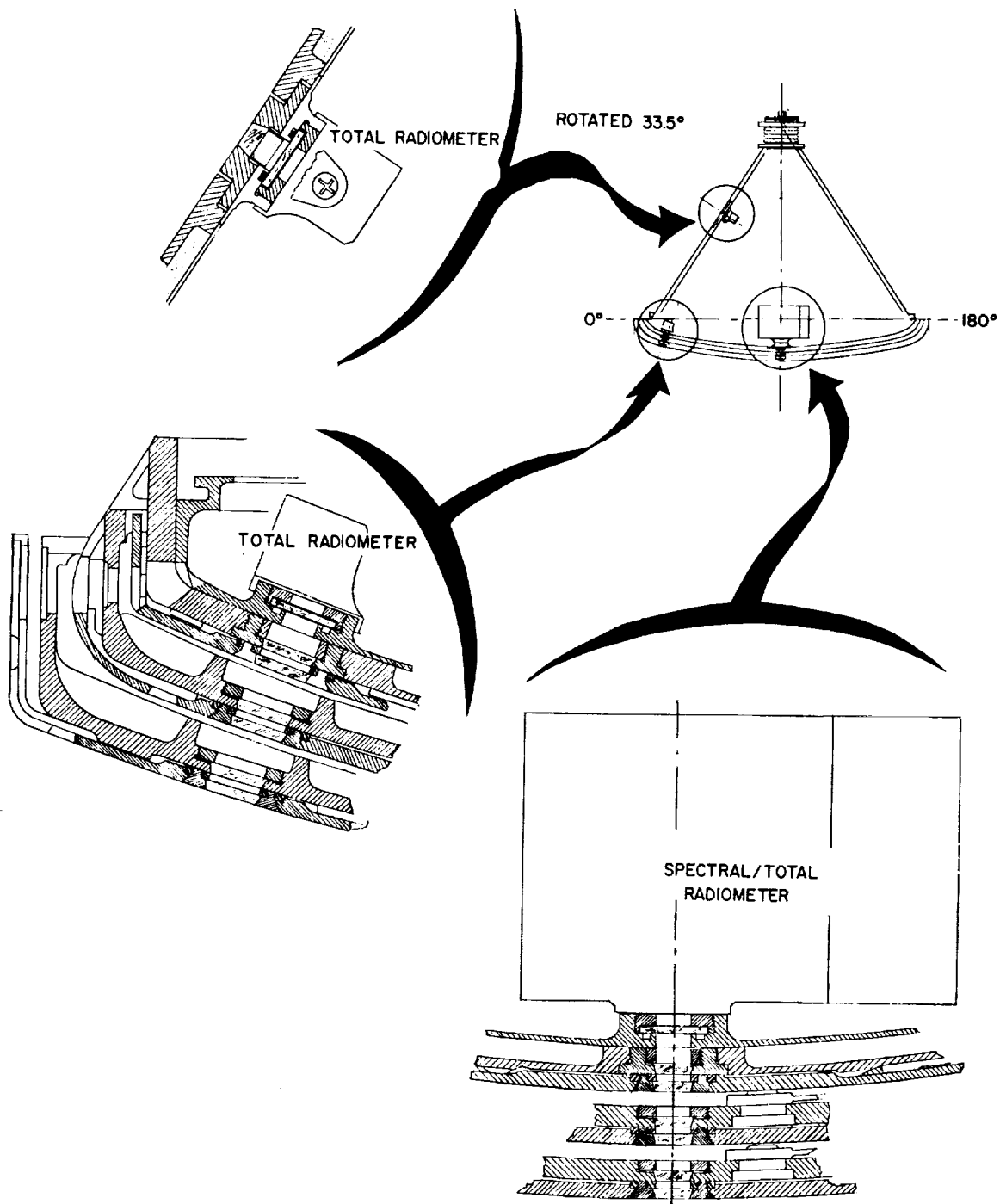
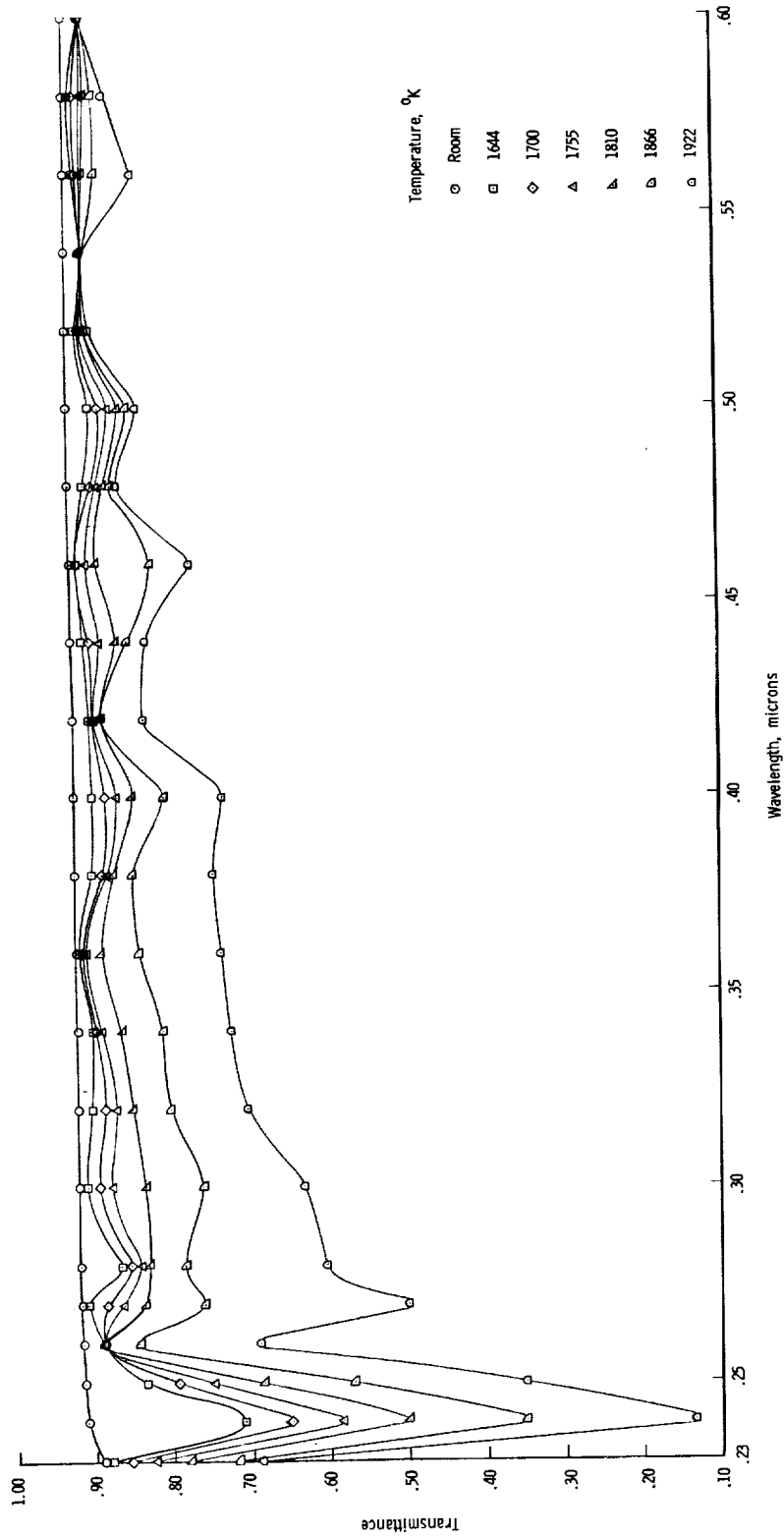
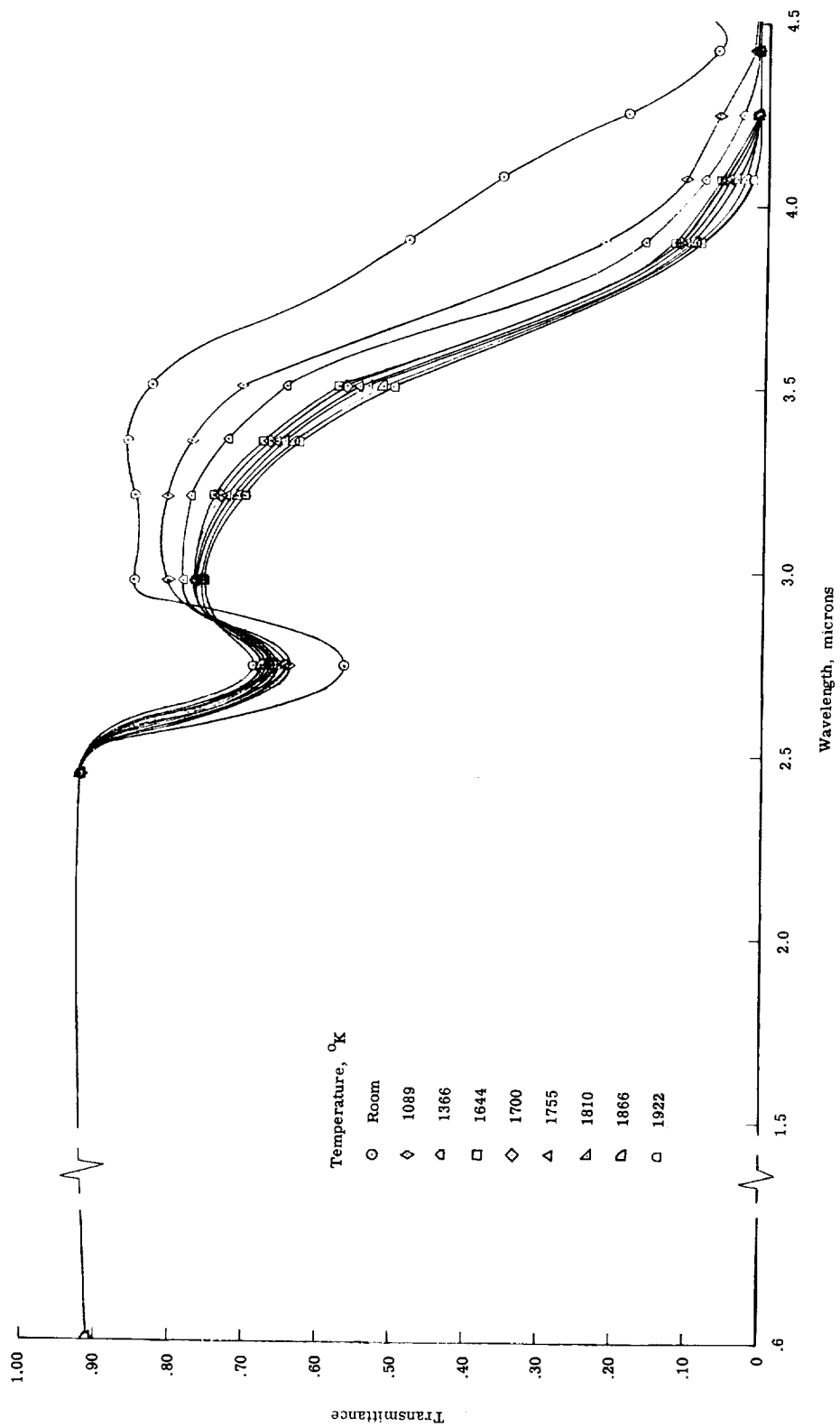


Figure 2.- Location of radiometers and windows.



(a) Wavelength, 0.23 μ to 0.60 μ .

Figure 3.- Transmittance of fused quartz as a function of temperature.
Thickness, 0.004 m.



(b) Wavelength, 0.6 μ to 4.5 μ .

Figure 3.- Concluded.

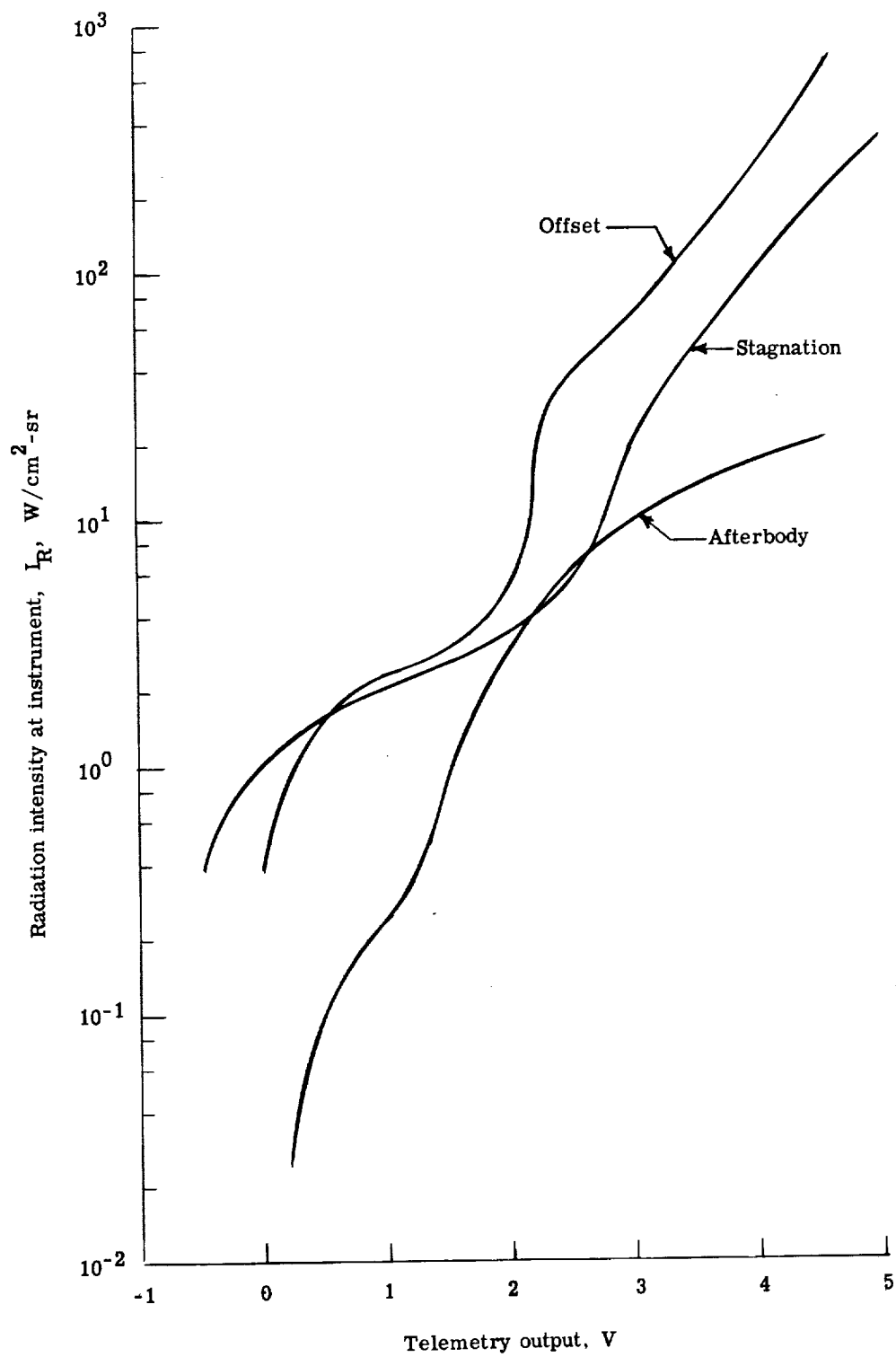
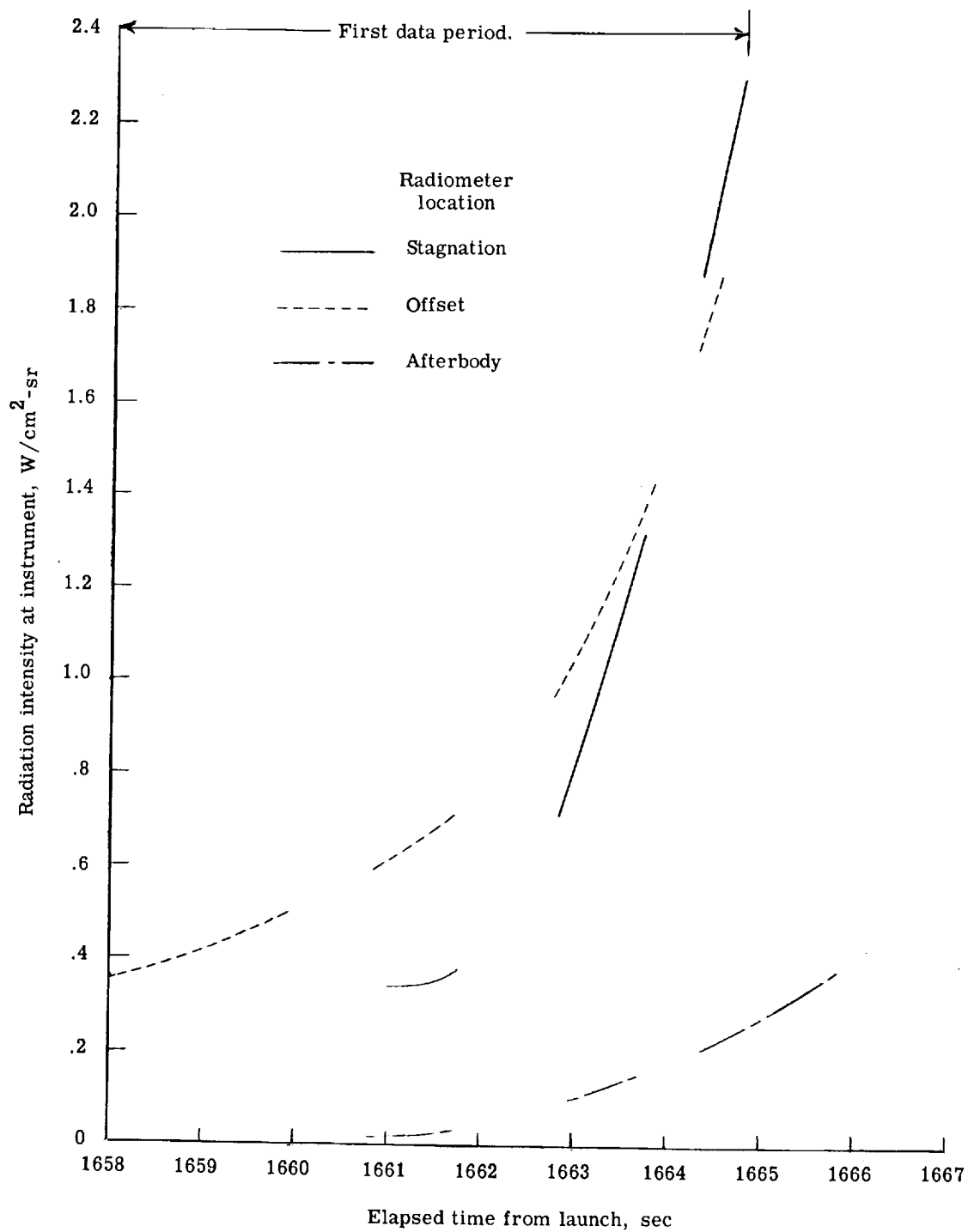
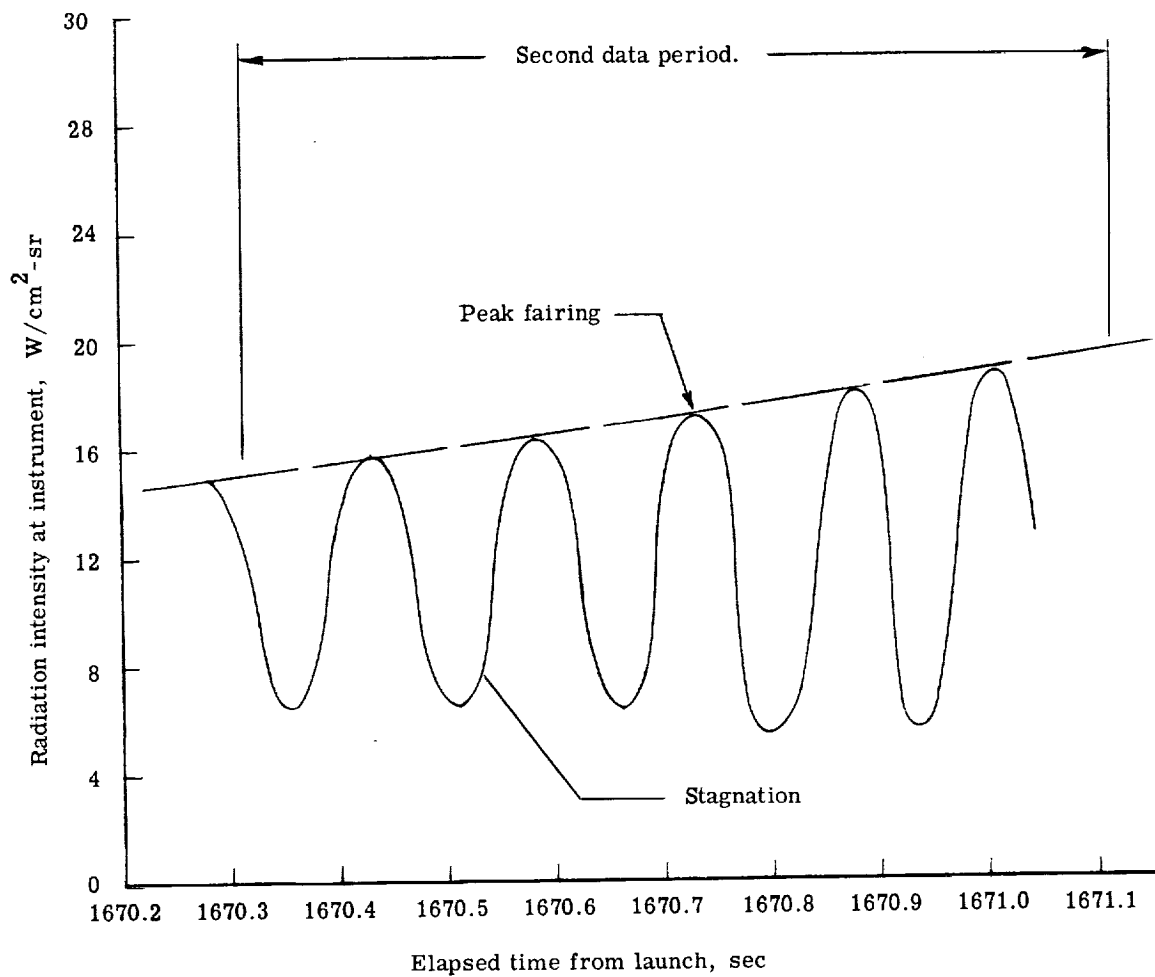


Figure 4.- Flight 1 radiometer calibrations.



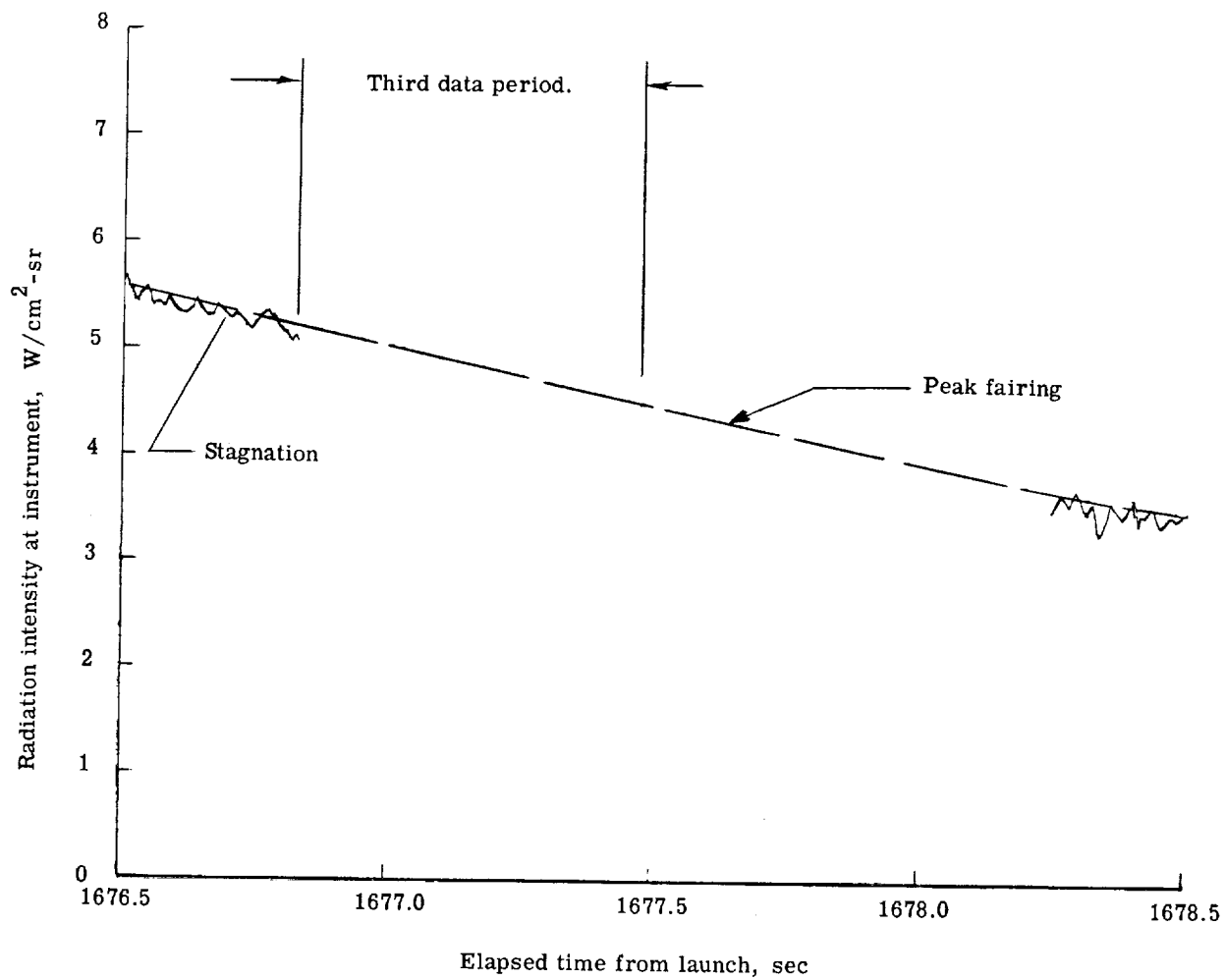
(a) First data period.

Figure 5.- Time history of radiometer data for Project Fire Flight 1.



(b) Second data period.

Figure 5.- Continued.



(c) Third data period.

Figure 5.- Concluded.

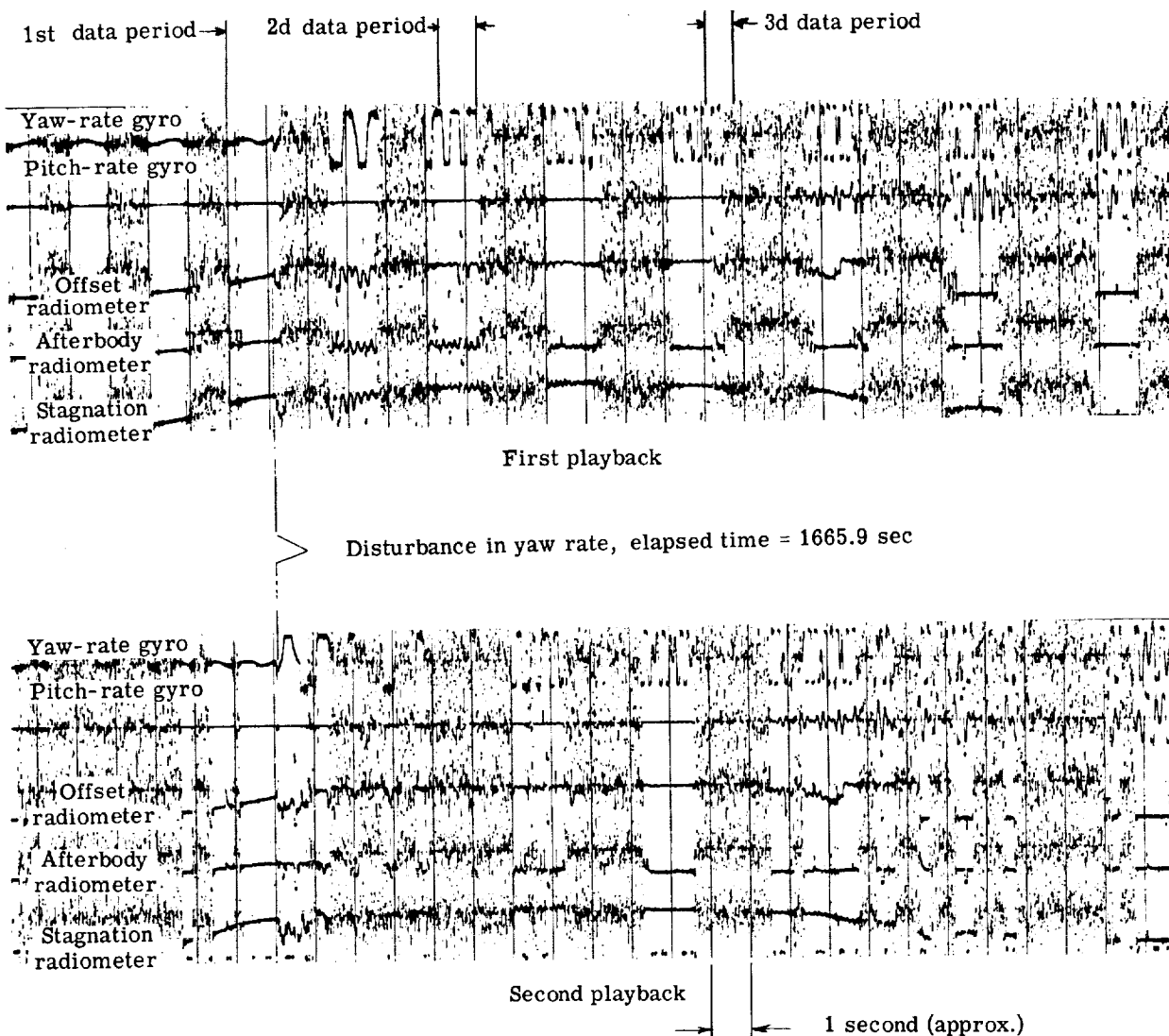
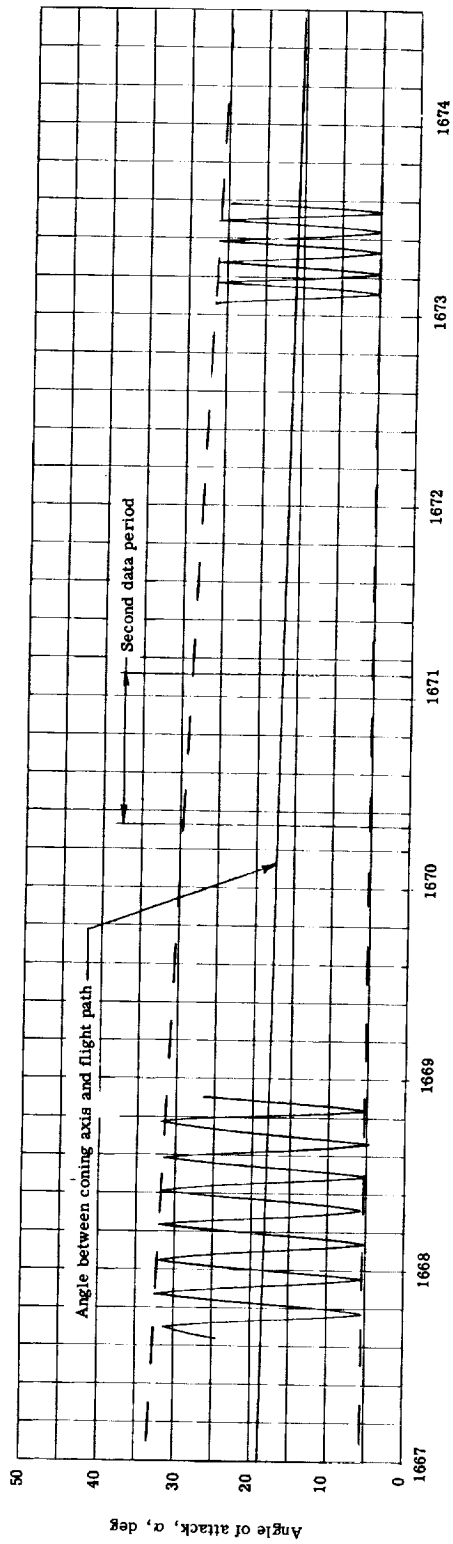
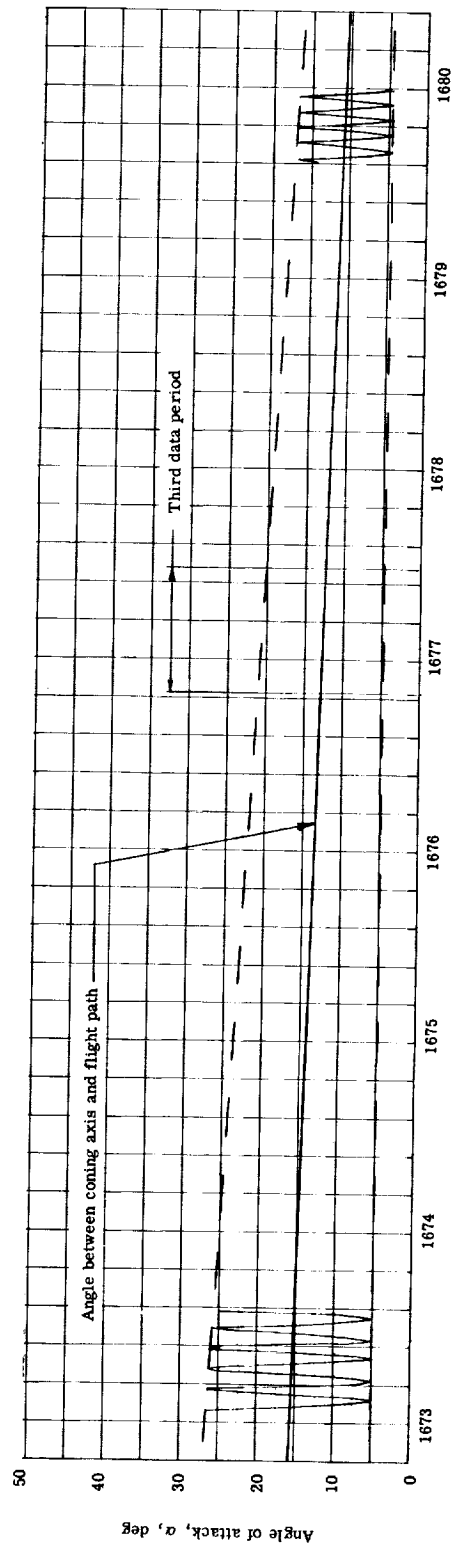


Figure 6.- Samples of the continuous channel telemetered data received by the Ascension Island TIM-18 station during the first and second playback transmissions.



Elapsed time from launch, sec



Elapsed time from launch, sec

Figure 7.- Calculated angle-of-attack history during Fire 1 reentry.

0374234.1300

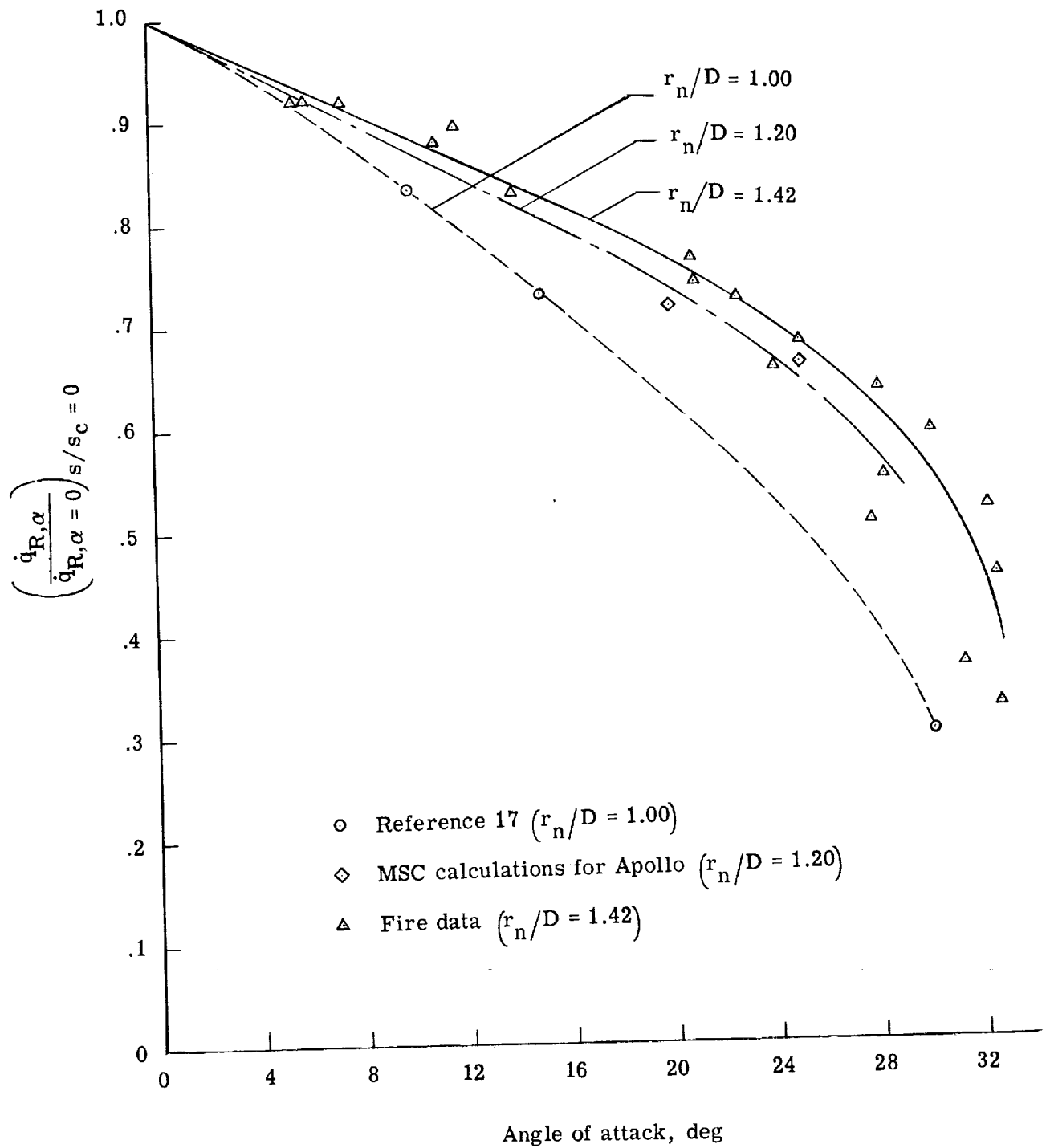


Figure 8.- Variation of radiative heating at the geometrical stagnation point with angle of attack for reentry vehicles with varying bluntness.

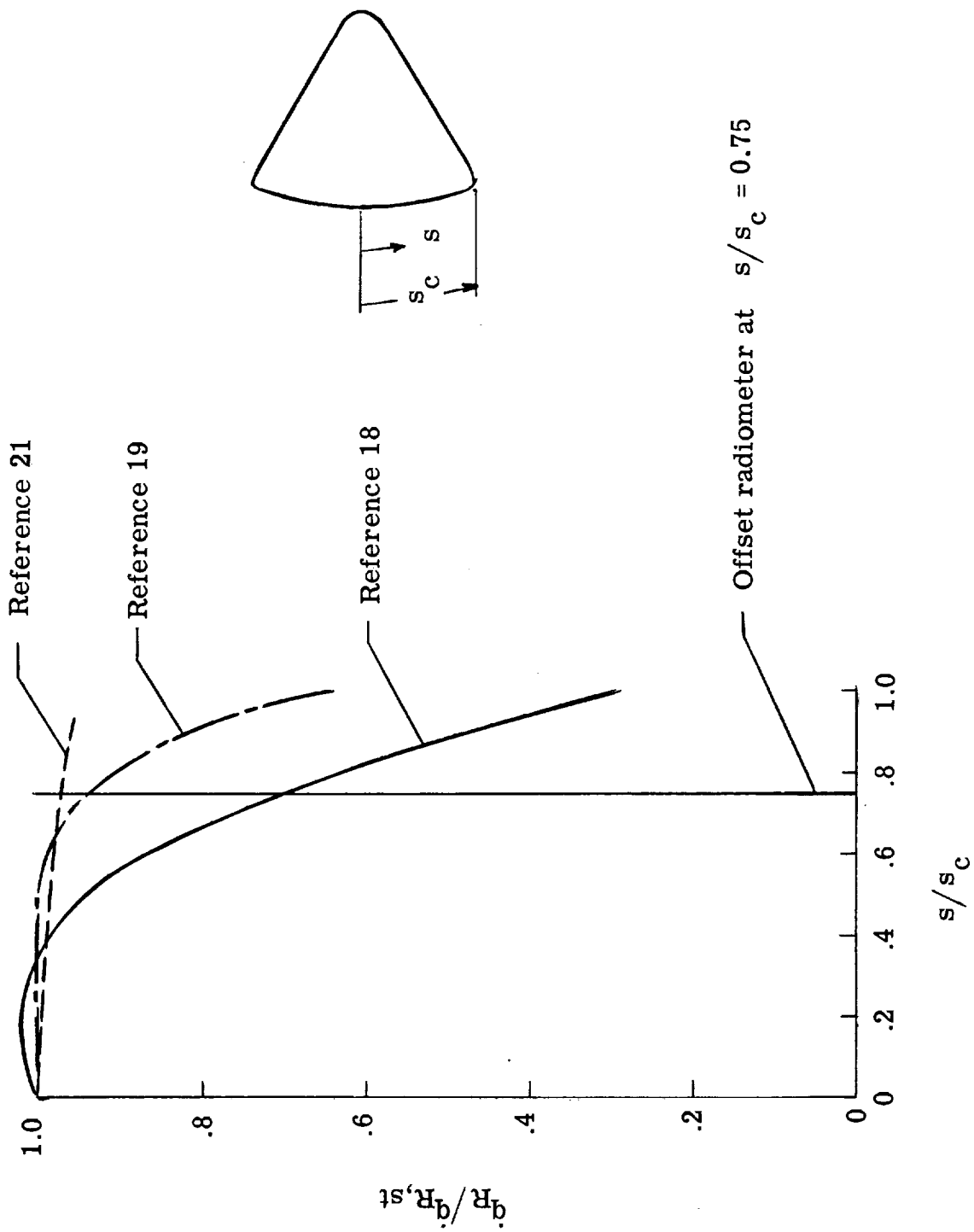


Figure 9.- Theoretical radiative heating distributions for a given early flight condition.

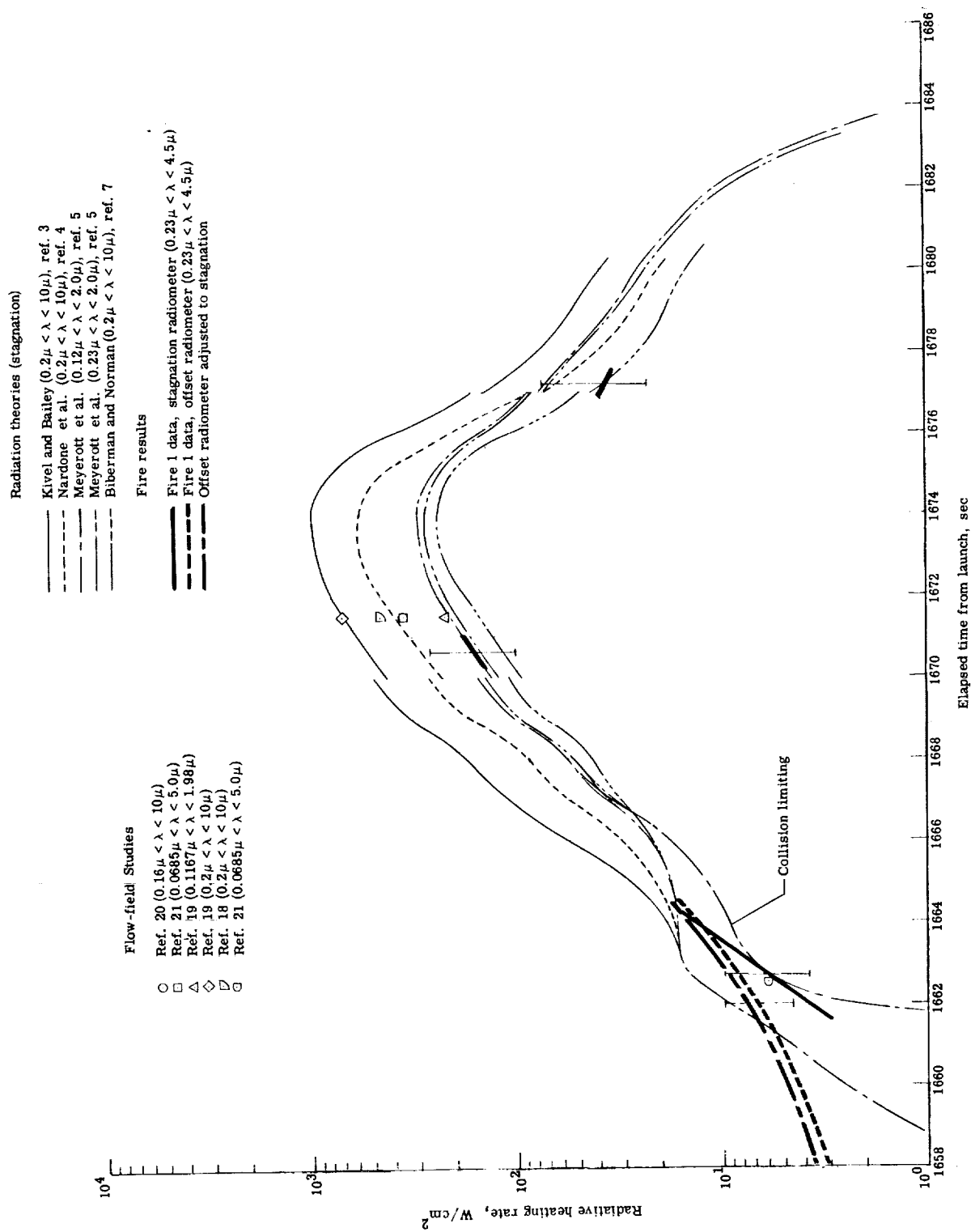


Figure 10.- Comparison of Flight 1 experimental and theoretical forebody heating rates.

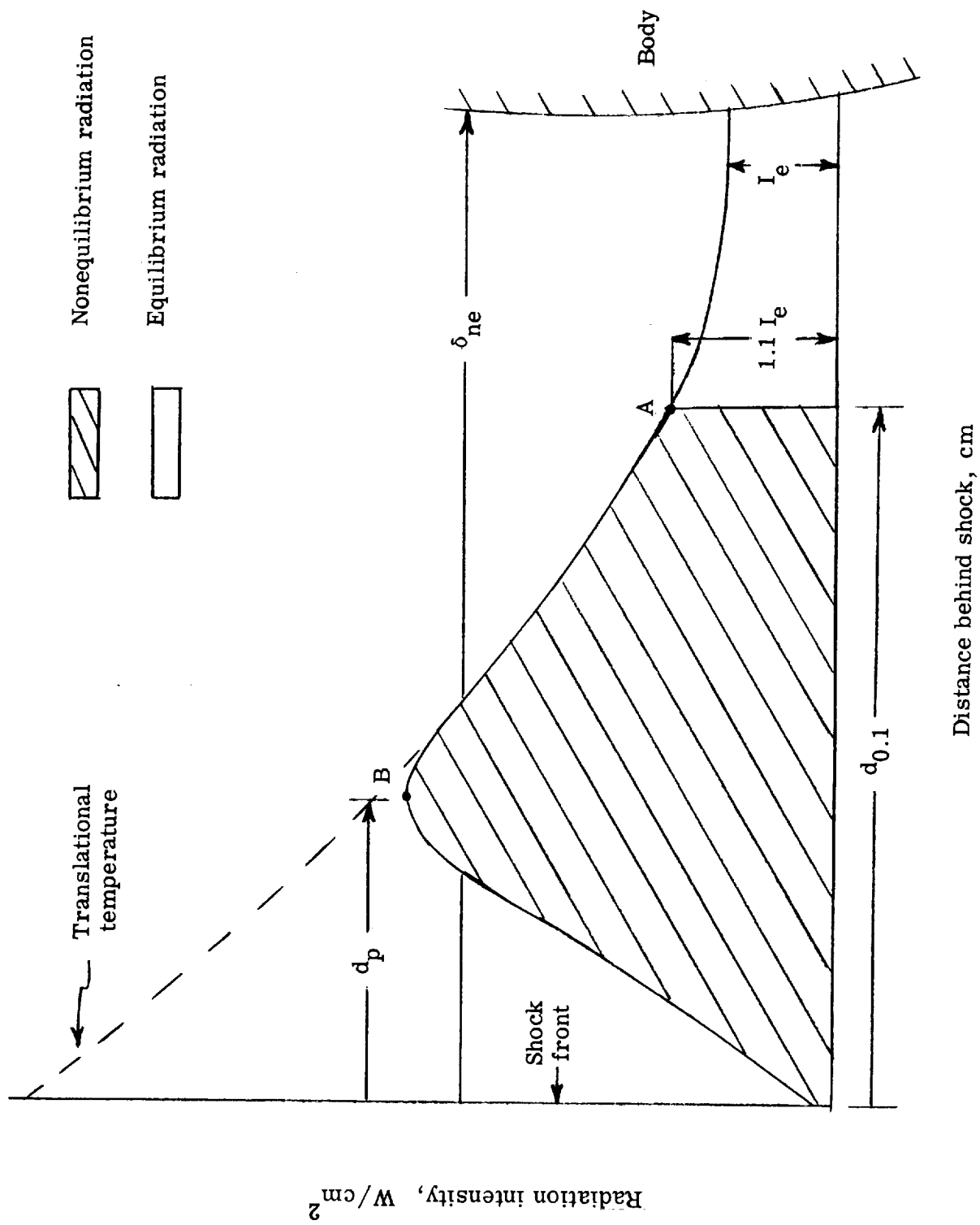


Figure 11.- Characteristic distribution of radiation between shock front and body.

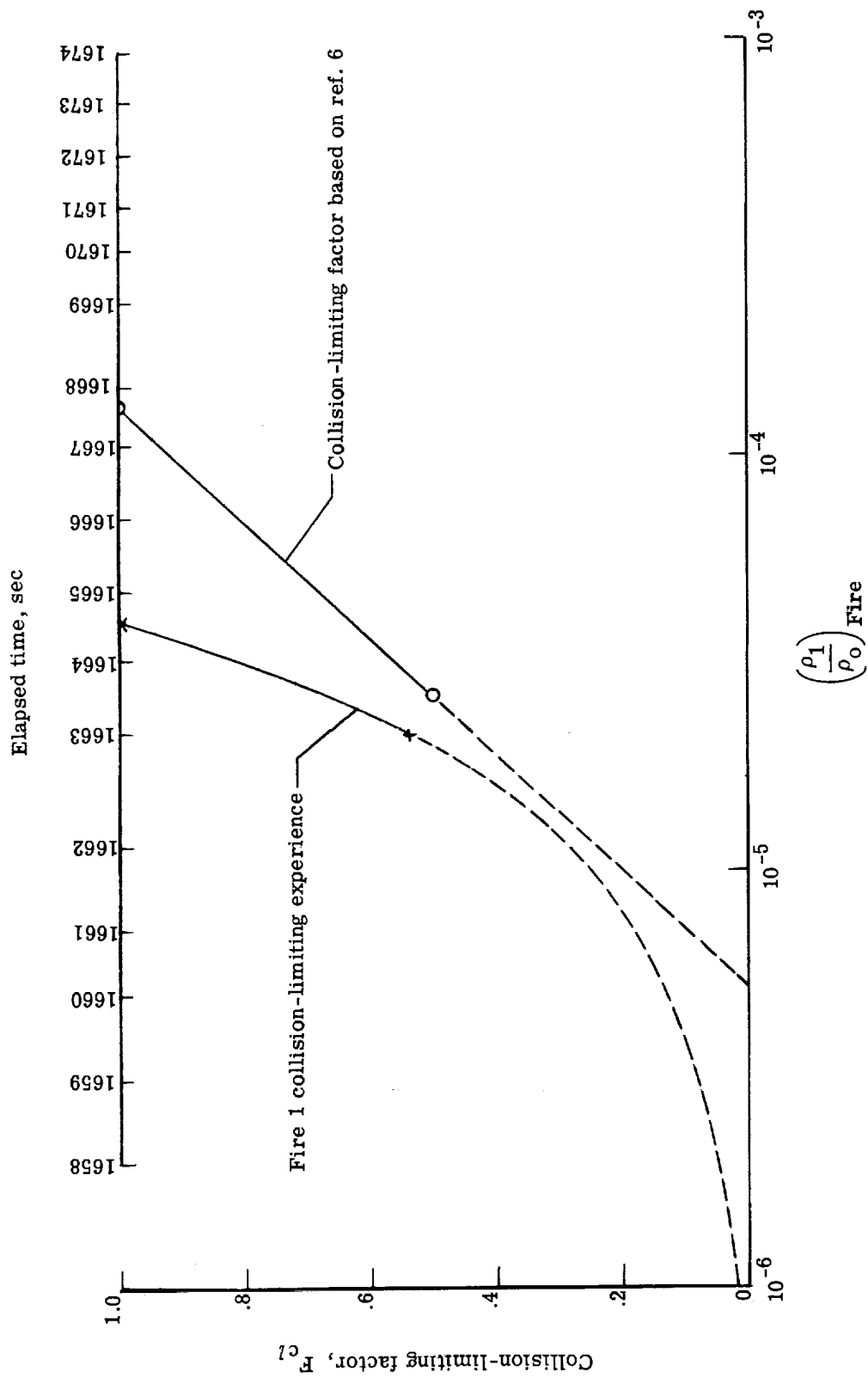


Figure 12.- Proposed collision-limiting factor for radiation during high-speed reentry.

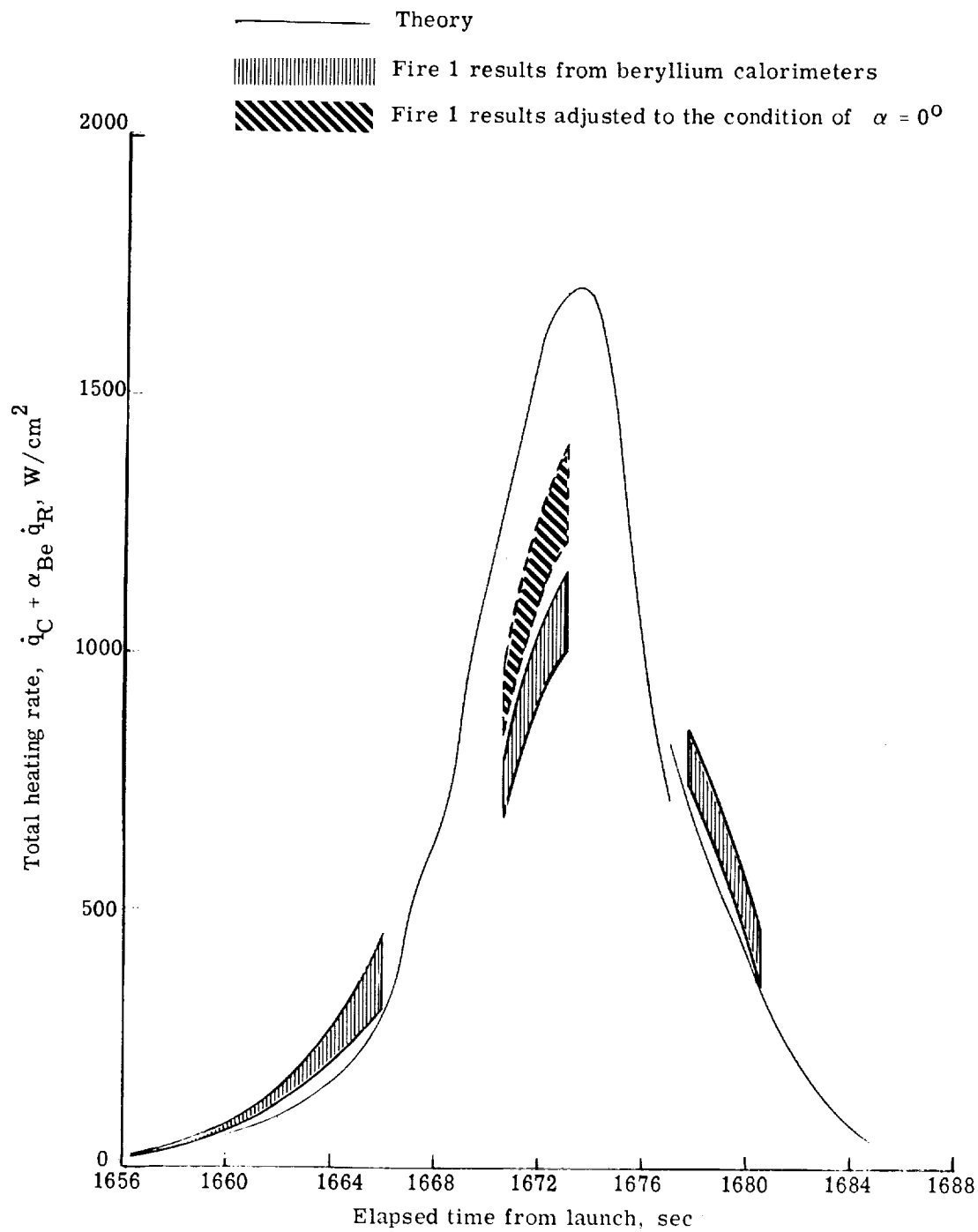


Figure 13.- Fire 1 experimental and theoretical stagnation total heating rates.

03744044

03744044



CONFIDENTIAL

CONFIDENTIAL